DOI: 10.1002/((please add manuscript number))
Article type: Full Paper

Functionalized Carbon Dots on Graphene as Outstanding Non-Metal Bi-Functional Oxygen Electrocatalyst

*Juhun Shin[1], Jian Guo[1], Tingting Zhao[1], and Zhengxiao Guo[1,2,3]**

[1] Department of Chemistry, University College London
20 Gordon Street, London, WC1H 0AJ, UK;

[2] Department of Chemistry and Department of Mechanical Engineering,
The University of Hong Kong, HK SAR;

[3] HKU Zhejiang Institute of Research and Innovation, The University of Hong Kong,
Lin'An, Hangzhou, P.R. China

E-mail: juhun.shin.10@ucl.ac.uk and z.x.guo@ucl.ac.uk

Keywords: carbon dots, bi-functional, oxygen electrocatalyst, metal-free, heteroatoms

Carbon-based bifunctional electrocatalysts for both oxygen reduction and evolution reactions are potentially cost-effective to replace noble-metals in energy devices such as fuel cells, metal-air batteries, and photoelectrochemical converters, but enrichment of active sites holds the key to efficiency. Here, graphene frameworks with heteroatom-doped carbon dots (CDs) are developed via a hydrothermal route followed by pyrolysis. The CDs are rationally prepared with careful selection of heteroatoms; embedded on the substrate to provide enriched active sites. Structural characterizations (e.g. TEM, XPS) reveal the successful addition of CDs with nitrogen and sulfur species. Especially, a heat treated N,S co-doped sample, NS-CD@gf_a900, exhibits the optimum oxygen electrocatalysis, even closer to noble-metal counterparts, as a result of the effect of active sites of the CDs and the synergistic behavior of N and S. Considering the importance of size and dopants of the material, this approach not only suggests a straightforward preparation route of nano-carbons, but also appoints the utilization of a new class of non-metal species as efficient oxygen electrocatalysts.

1. Introduction

In order to reduce the environmental impact associated with the combustion of fossil fuels, electrochemical energy storage has advanced significantly both in volume and in capacity, driven particularly by the electrification of transport and the development of smart electricity grids. Rechargeable ion batteries are currently under popular development, but limited by specific energy and power density due to limitations associated to ion-shuttling mechanisms at high applied current.[1, 2] Electrocatalysts are key components in clean energy conversion/storage devices including fuel cells, electrolyzers, and metal-air batteries.[3] The latter exhibits at least 5 times the theoretical specific energy of Lithium-ion technology, depending on the choice of metal, to be the next generation high energy source. The dominant processes involve oxygen reduction reactions (ORR) and oxygen evolution reactions (OER) at the cathode, a sluggish multi-electron transfer process.[4] Typically, platinum, ruthenium or iridium-containing species set the benchmark performance, but there are issues of scarcity, cost, fuel-crossover, and poor long-term stability.[2] Therefore, developing a stable and inexpensive electrocatalyst with enhanced kinetics (low associated overpotential) and activity remains as a challenge for possible commercialization of above-mentioned devices.

Catalysts based on transition metals and their oxides, carbides and nitrides have been investigated extensively as low-cost alternatives to precious metals, some of which show very promising performances[5], though issues with substrate binding and stability remains.[6]

More recent research has studied metal-free carbon-based materials with appropriate doping of heteroatoms, such as N, S, P and B, leading to low-cost systems with good cyclability over many existing transition metal species and even noble metals.[7] Especially, doping nitrogen into graphitic structure is a well-known procedure of introducing nitrogen functional groups as catalytically active (electron donating) sites by slightly adjusting the band-gap of the material - tuning the electronic properties with minimal structural alterations (e.g. graphitic nitrogen).[8, 9] Also, multi-functional groups by co-doping more than one heteroatom were reported to show synergistic effect towards ORR as metal-free catalysts.[10, 11]

Recently, carbon dots (CDs) of a few nanometer-scale have emerged as so-called zero-dimensional derivatives of carbon as potential substitute for many applications.[12] The nanoparticles have quasi-spherical morphology with varying size; the width up to 20 nm and the height ranging from few to multiple layers of carbon agglomerates.[13] CDs are synthesized from top-down and bottom-up approaches which consist of a mixture between sp^2 graphite-like and amorphous carbon.[14] Size- and edge-effect are vital in catalysis as the reaction generally happens near newly-introduced functional groups, which result in the formation of electron-rich and/or structural defect sites around the edge-planes.[15] CDs can provide more catalytically active sites by both surrounding edges and multiple layers, along with many functional groups.[16] However, despite the attempts of utilizing CDs in electrocatalysis[17], performance of CD-containing ORR electrocatalysts cannot reach the level of noble-metal catalysts and there are no reports exploiting OER with CDs. It is unclear if this unsatisfactory performance is due to the undefined-CD syntheses, binding of CDs to the substrate, substrate pore blockage, or the functional-groups around CDs.

In order to clarify the compatibility of CDs and the substrate, and the effect of different functional groups in CDs, we have designed heteroatom-doped CDs embedded on graphene substrates from a simple hydrothermal approach followed by heat treatment. Different combinations of heteroatoms (N, and N-S) CDs were prepared also by hydrothermal process with carefully selected reagents to exclude any other undesirable elements to the reaction. Obtained catalysts all showed considerable improvement in performance, as metal-free catalyst, only by the addition of CDs to the reaction mixture. After thermal treatment optimization, electrocatalytic activities in both ORR and OER regions were comparable to conventional Pt/C and Ir/C with extremely high current densities for a given catalyst loading.

2. Results and Discussion

The schematic synthesis procedures of heteroatom-doped carbon dots embedded porous graphene (CD@gf) are illustrated in **Figure 1**a. Heteroatom co-doped CDs, and highly porous CD@gf samples were prepared in bulk by a simple hydrothermal approach. The highly exfoliated GO sheets (Figure S1, Supporting Information) with abundant oxygen-containing functional groups were synthesized by an improved Hummers' method (described in the Experimental section).[18] Effective isolation of single-few layered GO was achieved by providing sufficient time for the oxidizing agent to diffuse fully into water.[19] Many oxygen-containing groups, including hydroxyl, and carboxyl (XPS results in Figure S2, Supporting Information) not only allow sufficient GO dispersion[20], but also provide sites for CDs to interact. This results in random re-assembling of reduced graphene oxide (folded, twisted, and wrinkled manner) where pores/defects of the hydrogel are occupied by the CDs to provide many catalytically active sites.[21]

Heteroatom doped CDs were successfully synthesized via simple hydrothermal-assisted condensation polymerization reactions. They are measured to be in the range of 3-20 nm in diameter, evidenced by AFM (Figure 1b and Figure S3, Supporting Information), and TEM results (Figure 1c and size distribution in Figure S4, Supporting Information). There is a wide diversity in the AFM height profile – from few layers to multiple layers/clumps of carbon. The structures are defined to be a mixture of amorphous and graphitic-like phase; this is shown by the interlayer spacing (100) of 0.24 nm (TEM in Figure 1d and the interspacing profile), 0.34 nm from reduced fast Fourier transform (FFT) image corresponding to the (002) lattice fringe of graphene, and the six-fold symmetry (inset of Figure 1d)[22] – graphitic structure also indicated by the presence of D-G bands in Raman spectra (Figure S5, Supporting Information)[23, 24], and broad observable peaks in XRD around 22 °, (002) facet[25], for all CD samples (Figure S6, Supporting Information). Incorporation of heteroatoms (all N, and S being bigger atoms than C with more available valence electrons) lead to increase in amorphous nature of graphitic plane which can be directly linked to more defect sites in the given structure.

XPS results provided the chemical properties of heteroatom-doped CDs; C 1s spectrum of NS-CD (Figure 1e) exhibited C=C, C-C, C-O, C=O, and O-C=O bonds at binding energies of 284.8, 285.4, 286.2, 288.1, and 288.7 eV, respectively.[24, 26, 27] Binding energies of heteroatom to carbon bonds (of N, and S) overlap with the energies of C-C and C-O bonds showing increase in fitted peak intensities. Surface heteroatoms (either N or N/S) are revealed by the survey scans where the contribution of sulfur shifts the C 1s spectrum of NS-CD to higher energy than of N-CD (Figure S7, Supporting Information). The N 1s spectrum (Figure 1f) demonstrates the presence of pyridinic N (~399.5 eV), pyrrolic N (~400.3 eV), and graphitic N (401.7 eV), suggesting that sp^2/sp^3 nitrogen species are generated during the reaction. Energies of amine group ($-NH_2$) overlap with pyrrole groups and are omitted.[28-30] Binding energies of sulfur are around 162.4, 163.6, 164.8, and 167.0 eV corresponding to thiol group (S-H) on the surface, thiophene-S (C-S, C=S, spin-orbit coupling of S 2p), and sulfur oxide (SO_X) as shown in Figure 1g.[28, 30] O 1s high-resolution spectrum (Figure S8, Supporting Information) indicates C=O, C-O, O-C=O, and S=O bonds at 530.8, 531.5, 532.1, and 533.6 eV, respectively.[26, 28] Such bonds are also evidenced by the ATR results (Figure S9, Supporting Information); observed N- or S- containing (1655, 1384/1172 cm^{-1} of C=N/C-N, and 1179, 644 cm^{-1} of C=S/C-S) heterocycle stretching vibrations[31] and suggest the existence of the heteroatoms within carbon structures in accordance with the XPS results. The dopant concentration and the percentage of N species (Table S1, Supporting Information) suggest that the bigger sulfur atoms govern the amount of nitrogen groups formed around the edges – reducing the concentration of edge-populating pyrrole/amine group.

High intensity (001) plane at around 11.1 ° of GO and (002) plane of graphite are shown in the XRD results (Figure 2a). RGel, NS-CD@gf, and NS-CD@gf_a900 samples all exhibit rather broad (002) peaks around 21.0 °, indicating an overall amorphous nature but varied short-range order of the reassembled graphene sheets. The effect of incorporated CDs broadened the (002) peak than the sample without. Further fragmentation and defect formation of carbon during annealing can be seen by the broadened (002) peak. (100) plane is shown for all samples at roughly 42.0 °. Raman spectra (Figure 2b) show 0.86, 0.93, and 1.08 I_D/I_G ratio of RGel, NS-CD@gf, and NS-CD@gf_a900, respectively. Close values of RGel and NS-CD@gf suggest that there are no major changes in defect chemistry with the embedded CDs. Whilst, the observable increase in the I_D/I_G ratio, compared to untreated, is seen with the annealed sample which can be attributed to the formation of hierarchical porous structures of carbon with more defect sites available.[32] N_2 adsorption-desorption isotherm (Figure 2c) confirms the BET surface area of 264.66 and 559.59 $m^2 g^{-1}$ respectively for NS-CD@gf, and NS-CD@gf_a900 with micro- and meso-pores present.[33] General pore opening, as mentioned before, is displayed with increase in pore diameter across all range (Figure S11, Supporting Information). All BET specific surface area and pore volume are represented in Table S2 (Supporting Information).

Embedment of CDs is demonstrated by direct comparison of the physical size of hydrogels; significantly larger dimensions of NS-CD@gf than of RGel sample (photo, Figure 2d). Both SEM (Figure S12, Supporting Information) and TEM (Figure 2e; Figure S13, Supporting Information) images reveal highly porous and fragmented carbon frameworks to facilitate easy penetration of oxygen molecules during electrocatalytic processes. Generally, to prepare a hierarchically porous carbon, a template is used which then requires additional non-environment friendly etching process.[34] Instead, use of highly exfoliated graphene leads to a simple effective way of preparing porous substrates. Embedment of CDs to a graphene substrate is confirmed in low and high magnification TEM images (Figure 2e, f); CDs can be observed as particles with darker contrast either around the edges or the voids on the plane of the graphene layer. Same region TEM-EDS elemental mapping (Figure 2 g-j) of nitrogen and sulfur further illustrates the presence of NS-CDs and the heteroatoms on carbon. XPS results of the CDs embedded graphene and thermally treated samples show change in overall composition of elements (as shown in Table S3, Supporting Information). Atomic weight % of both N and S decrease for annealed samples as thermally unstable/weak bonds (-NH_2, and -SH) break at high temperature. Comparison of high resolution N 1s and S 2p scans validates the alteration in heteroatom environment (Figure S14, S15, Supporting Information).[35] Decrease in oxygen functionalities can also be highlighted by the oxygen composition change in Table S3 and the C 1s spectra in Figures S14 and S15. Although the concentration of graphitic N (most responsible for lowering the overall free energy of ORR) in CDs and the total amount of heteroatoms are not significantly high compared to some reported literature, effective embedment of CDs together with the effects of dual-heteroatom doping (N, and S) boost the overall catalytic performance.

All samples are used directly as synthesized and electrochemically tested to understand the materials' potential as cathodes for metal-air batteries. The ohmic potential drop has not been applied to any of the tests (not iR-corrected). Initially, CV scans are measured in N_2/O_2 saturated 0.1 M KOH electrolyte. Distinct oxygen reduction peaks are shown only when oxygen is purged to the electrolyte solution (Figure 3a) suggesting a successful oxygen redox reaction. Reduction peak current of the Pt/C sample is at 0.82 V vs. RHE whereas the peak of the NS-CD@gf_a900 sample is around 0.71 V. Differences in current densities (of O_2 and N_2) from CV scans are 1.25 and 1.53 mA cm^{-1} for Pt/C and NS-CD@gf_a900, suggesting that the CD doping enhances the electrical response. Linear sweep voltammetry (LSV) curves of all N-CD@gf, NS-CD@gf, N-CD@gf_a900, and NS-CD@gf_a900 samples exhibit outstanding electrocatalytic activities in an alkaline solution, with current responses either similar to or greater than Pt/C, despite being metal-free (Figure 3b). The performance of the NS-CD sample is as expected due to its low active material-to-electrode surface coverage and poor conductivity from high oxygen functionalities.[36] Although the on-set potential (E_{onset}) and the half-wave potential ($E_{1/2}$) of NS-CD@gf_a900 are approximately 0.93 and 0.75 V (slightly lower than of Pt/C at 0.98 V, and 0.84 V), the limiting current density is 7.71 mA cm^{-1} at 1600 rpm in 0.1 M KOH electrolyte, surpassing all CD embedded samples and even higher than the 5.55 mA cm^{-1}, Pt/C current response (approximately 38%) – current measured at $E_{1/2}$ also greater. Note that both thermally treated CD (N, and NS) embedded samples exceed the limiting current density of Pt/C; performance enhancement of catalysts realized by the intrinsic catalytic activities of CDs. The same trend is observed for the ORR results of CD@gf, and CD@gf_a900 samples; NS-dual-doping exhibits the highest activity followed by the single N-doping. RDE-LSV measurements were collected at different rotation speeds (Figure 3c). NS-CD@gf_a900 outperformed all counterparts at any rotation speed, and the performance was comparable to the Pt/C benchmark (Figure S16, S17, Supporting Information). K-L relations can be extrapolated from measured current densities of different rotations (in the inset of Figure 3c; and Figure S15, Supporting Information). Steady linear slopes suggest that the reaction kinetics is of first-order, with respect to the dissolved oxygen concentration in the electrolyte system. The n value, electron transfer number, of NS-CD@gf_a900 is calculated to be around 3.96 (approaching 4, theoretical value at a successive $4e^-$ reduction pathway) for the potential range of 0.2-0.5 V vs. RHE, implying effective oxygen reduction reactions. K-L values of N-CD@gf_a900 and Pt/C are 3.89 and 3.73, respectively; again, a high electron transfer number is obtained by the annealed N-CD carbon sample. The initial small hump in the ORR in low rotation suggests the peroxides formation however, gradually decreases with the increase of oxygen feed – approaching stable $4e^-$ processes.[37] Tafel slopes of all samples were obtained to study the relationship of the rate of ORRs with the attained overpotentials (Figure 3d). The value for the Pt/C (76.1 mV/dec) is smaller than the rest suggesting that the oxygen adsorption process is fast on the surface of the Pt/C. Still, the values of N-CD@gf_a900 and NS-CD@gf_a900 are 83.3 and 83.2 mV/dec, very close to that of Pt/C. The Tafel values of N-CD@gf and NS-CD@gf were 93.1 and 82.4 mV/dec, respectively.

To validate the effect of CD embedment on catalysis, the RDE result of NS-CD@gf_a900 is compared to the NS-Gel_a900, annealed-direct-heteroatom-doped graphene gel samples with no CDs (Figure 4a). The observed ORR overpotential of the direct heteroatom-doped sample (E_{onset} = 0.94 V) is only slightly smaller than the CD-containing samples, but the measured current density is only about half (~4.46 mA cm^{-2}) of the latter - which in fact is even lower than that of the untreated N-CD@gf and NS-CD@gf. It can be presumed that the direct heteroatom-doped defect sites are more accessible for the bulk oxygen migration and hence, lead to a low overpotential.[38] Yet, a high number of vacant active sites can be provided by rich core/edge doping of heteroatoms in CD embedded graphene framework resulting in improved ORR activity. Also, to understand the influence of annealing temperature, the RDE results of NS-CD@gf_a800, NS-CD@gf_a900, and NS-CD@gf_a1000 were studied (Figure 4a). Slight increase in the activity is shown at carbonization temperature of 800 °C with improved diffusion properties (compared to the untreated sample). However, it can be assumed that at 800 °C there are still some oxygen functionalities interfering with the performance as well as the low conversion ratio of graphitic N.[39] At 1000 °C, on the other hand, despite the increase in rate of conversion with 60 mV reduction in overpotential (low oxygen, and high graphitic N), the loss of sulfur containing groups (Table. S4 and Figure. S18, Supporting Information) results in no-change in limiting current density, compared with 800 °C.[40] The optimum temperature of annealing is at 900 °C with the oxygen level low enough to give rise to good conductivity and high graphitic N concentration whilst preserving sulfur components in CD-graphene materials.

The amount of CD embedment was varied in order to clarify the effect of the active site densities provided by the CDs. As shown in Figure S19 (Supporting Information), when the amount of NS-CD used is halved in the NS-CD@gf_a900(s) sample, the current response is significantly reduced with E_{onset} at 0.86 V compared to the original sample (NS-CD@gf_a900). As the addition of NS-CD is doubled in the sample, NS-CD@gf_a900(h), the current density and E_{onset} increase slightly to ~5 mV cm^{-2} and 0.88 V, respectively. The SEM images of the following samples (Figure S20, Supporting Information) show that the morphologies of the graphene substrate are more or less the same when the CD amount is halved. This suggests that the reduction of electrocatalytic performance for the halved sample is governed by the decreased number of active sites; for the same reason, the E_{onset} of NS-CD@gf_a900(h) is slightly higher than NS-CD@gf_a900(s) sample. However, as the amount is doubled, the pores of the graphene start to close-up, as noted in the high magnification image of NS-CD@gf_a900(h) as shown by the BET surface area and pore volume (Table. S5, Supporting Information). This may be due to agglomeration of CDs around the pores and edges of graphene sheet, hence restricting the access to some of the active sites within.

To evaluate the OER feasibility, all CD containing samples were tested for OER activity in an alkaline solution – in the potential range of 1.2-2.0 V vs. RHE at a rotation speed of 1600 rpm (Figure 4b). E_{onset} values are all either very close to or less than 1.6 V. It is clear that NS-CD@gf_a900 sample has the lowest overpotential and the highest current response over the tested potential range, compared with other catalysts. E_{onset} and the potential at 10 mA cm^{-2} for a given catalyst (E_{j10}) of NS-CD@gf_a900 are 1.52 and 1.68 V, respectively, compared to 1.48 V and 1.58 V of Ir/C in 0.1 M KOH. Interestingly, the contribution of sulfur is apparent towards the OER performance. In CD@gf samples, the minor influence of sulfur only increases the activity of NS-CD@gf by a small amount, compared with N-CD@gf. However, after thermal treatments of the gel samples, a notable enhancement of NS-CD@gf_a900 OER activity is realized (30 mV, and 60 mV difference in E_{onset}, and E_{j10} compared to N-CD@gf_a900). The corresponding Tafel slope of NS-CD@gf_a900 (87.5 mV/dec) also confirms the best rate of OER against 460, 448, 208, 126, 106 mV/dec of NS-CD, RGel, N-CD@gf, NS-CD@gf, and N-CD@gf_a900 catalysts (Figure S21, Supporting Information), respectively. A high concentration alkaline electrolyte can promote OER processes as the concentration of hydroxyl ions increase. In 1.0 M KOH, NS-CD@gf_a900 exhibits exceptional OER activity with 1.49 V (E_{onset}) and 1.59 V (E_{j10}); approximately 100 mV less overpotential than at 0.1 M KOH solution, and comparable OER performance to that of Ir/C – also, very close Tafel value (58.3 to 54.1 mV/dec of Ir/C).

The influence of CDs and the dopant elements, N and S, have been investigated. Substituting heteroatoms (slightly different electronegativity compared to carbon) alter the surface charge densities of graphene. With electronegativity higher than carbon, nitrogen groups can draw charge density towards them from neighboring carbons. The effect of the electron lone-pairs on the graphitic and pyrrolic nitrogen (electron donating) together with slightly positive carbon sites make oxygen adsorption more viable.[8] In the case of sulfur, similar electronegativity to carbon leads to imbalance orbital states, which contributes to high spin density of surrounding carbons.[41] Other studies also suggest that further reduction in adsorption energies for N, S-dual doping where carbons located adjacent to graphitic N and thiophene S exhibit the maximum spin density – responsible for ORR activity.[10] In contrast, OER activities are facilitated by pyridinic nitrogen (electron-withdrawing group) together with edge thiophene groups; the rate of adsorption of the negatively charged water oxidation intermediates (OH^-, and OOH^-) is favored.[42] Heteroatom-functional groups in CDs provide many catalytically active centers in given defect sites.

Long-term ORR current response of the NS-CD@gf_a900 is obtained from chronoamperometric curve in Figure 4c; NS-CD@gf_a900 more stable than of Pt/C with current retention kept to 88% compared to 73% after 60000 s. This further suggests that CD embedment induces ORR capabilities with good regeneration of electrocatalysts under constant oxygen reduction. This is also the case for the stability of OER as shown in Figure S22 (Supporting Information). In Figure 4d, the oxygen bifunctionality of N-CD@gf_a900 and NS-CD@gf_a900 samples are evaluated against the results of the (Pt/C+Ir/C) pair. Overall performances of CD embedded samples are slightly low on both ORR and OER compared to the combined noble catalyst. However, the ΔE values (potential difference between 3 mA cm^{-2}, ORR, and 10 mA cm^{-2}, OER) obtained are 0.99 V (N-CD@gf_a900), and 0.91 V (NS-CD@gf_a900) against the Pt/C+Ir/C (0.77 V). The value is further reduced to 0.82 V for NS-CD@gf_a900 (in 1.0 M KOH), comparable to many transition-metal containing oxygen electrocatalysts as well as metal-free carbon materials (Table S6, Supporting Information).

3. Conclusion

In summary, an outstanding metal-free porous graphene framework with the embedment of heteroatom-doped carbon dots as bifunctional oxygen electrocatalysts for metal-air batteries have been developed via a facile and scalable hydrothermal approach and subsequent annealing process. Prepared sample, NS-CD@gf_a900, exhibited substantial increase in the catalytic behavior (38% increase in current density) and stability (current attenuation of 12%) that is comparable to the performances of benchmark oxygen electrocatalysts (Pt/C+Ir/C). The synergistic integration of dual-N-S doping lowers the activation barrier for oxygen molecule adsorption on carbon. However, rather than occupying defect sites of highly porous graphene with a few number of dopants, embedding carbon dots provide numerous active centers, generated by nitrogen and sulfur species. This strategy of controlling the size/functional groups of carbon can be readily scaled-up and applied to improve and develop cost-effective metal-free oxygen electrocatalysts to replace noble-metal catalysts for large-scale energy storage and conversion systems.

4. Experimental Section

Materials: Citric acid (99%, Sigma-Aldrich), dicyandiamide (99%, Sigma-Aldrich), thiourea (99%, Sigma-Aldrich), graphite (<20 micron, Sigma-Aldrich), sulphuric acid (95-97%, Merck KGaA), phosphoric acid (>85 wt.%, Sigma-Aldrich), potassium permanganate (≥99%, Sigma-Aldrich), hydrogen peroxide (30 wt.%, Sigma-Aldrich), hydrochloric acid (35%, VWR), Nafion (5 wt.% in alcohol and water, Sigma-Aldrich), and 20% platinum on carbon black (Alfa Aesar) were directly used as received with no additional modification or treatments.

Synthesis of heteroatom-doped CDs: All CDs were prepared by a one-pot hydrothermal process: in a typical N-doped CD synthesis, 15 mmol of citric acid (CA) and 15 mmol of dicyandiamide (DCDA) were dissolved in 15 ml of deionized water (DI) and sonicated for 30 min. The resulting solution was then transferred into a 50 ml Teflon-lined stainless-steel autoclave and heated at 180 °C for 6 h. Collected solution was washed with methanol several times to remove unreacted species. Large agglomerated particles were separated using 0.22 μm pore filter membranes. Afterwards, filtrate was completely dehydrated at 100 °C for 24 h and grinded to obtain fine powder. N, S co-doped CDs were prepared only by changing the precursor to thiourea (TU). Samples were named as N-CD and NS-CD, respectively.

Synthesis of heteroatom-doped CD embedded graphene hydrogel: Graphene oxide (GO) was synthesized by oxidation of graphite using a reported improved Hummers' method.[18] A mixture of concentrated sulfuric acid and phosphoric acid (9:1 volume ratio) was stirred and cooled to < 5 °C. With vigorous stirring, graphite powder (5 g) was added to the acid mixture. Keeping the temperature below 10 °C, potassium permanganate (6 wt. equivalent) was slowly added. After the addition, the mixture was heated to 50 °C for 24 h. 600 ml of DI was added carefully with the temperature kept below 80 °C, followed by the addition of approximately 40 ml of hydrogen peroxide solution. Obtained slurry mixture was thoroughly washed in

3.4 % HCl then with water. GO mixture was freeze-dried to obtain light-brown powder. Obtained GO powder was added to DI and ultrasonicated for 2 h to obtain homogeneous GO solution (5 mg/ml). 20 mg of desired CD was added to 20 ml of former GO solution and sonicated for 30 min and was subjected to hydrothermal reaction at 180 °C, 12 h. Resulting reduced GO hydrogel was washed with DI a few times and freeze-dried. Samples were named after the CDs used in the reaction; N-CD@gf, and NS-CD@gf. Hydrogel formed with no CD was named as RGel.

Thermal treatment of CD embedded graphene hydrogel: Annealing processes were conducted at various temperature (800, 900, and 1000 °C) for 3 h under N_2 flow with 3 °C/min temp. ramping rate. Samples were named as CD@gf_aXXXX (where XXXX denote target temperature used).

Structural Chracterization: X-ray diffraction (XRD) patterns were collected between 2-60 ° using a STOE Stadi-P (Cu-Kα radiation, λ = 1.5406 Å). X-ray photoelectron spectra (XPS) were obtained using a Thermo Scientific K-alpha (Al source, 1486.6 eV). Scanning electron microscopy (SEM) images were taken using a JEOL JSM-6301F instrument. Transmission electron micrographs (TEM) and energy dispersive spectra (EDS) were recorded on a JEOL JEM 2100 (LaB_6 filament) and an Oxford Instruments X-MaxN 80-T Silicon Drift Detector (SDD) fitted to TEM machine. Raman spectra were obtained from using Renishaw Ramascope (514.5 nm laser). Atomic force microscopy (AFM) images were attained by Keysight Technologies 5600LS AFM instrument. Attenuated total reflectance infra-red spectra (ATR-IR) were collected using Bruker Tensor 27 FTIR spectrometer. Brunauer-Emmett-Teller (BET) isotherms of nitrogen adsorption-desorption were measured using Quantachrome Autosorb-iQC at 77 K, liquid N_2.

Electrochemical Characterization: All electrochemical tests were carried out at room temperature using Metrohm Autolab PGSTAT302N with a three-electrode system; Ag/AgCl (in sat. KCl) reference electrode, carbon rod as a counter electrode, and a glassy carbon (GC) coated working electrode where material of interest was casted on the surface. KOH (0.1 M) electrolyte was saturated by O_2 or N_2 purge prior to the measurements. Bubbling of either O_2 or N_2 was kept the same to maintain saturation. For the preparation of active catalyst, 2 mg of sample was added to 480 µl DI and 20 µl Nafion mixture and sonicated for 1 h to achieve homogeneous ink. 5 µl of the ink suspension was drop-casted on the GC tip (3 mm dia.) and dried at 60 °C. Active catalyst loading was fixed to ca. 0.28 mg cm^{-2} for all samples. Cyclic voltammograms (CV) were performed between -0.8 to 0.2 V vs. Ag/AgCl with a scan rate of 10 mV s^{-1} for 10 cycles. Linear sweep voltammograms (LSV) were recorded using rotating disk electrode (RDE, Metrohm) at the potential range of -0.8 to 0.2 V vs. Ag/AgCl system with sweeping voltage of 10 mV s^{-1} and varying rotation speed, 400, 800, 1200, 1600, and 2000 rpm, to study ORR capabilities. OER measurements were taken at the potential range of 0.2 to 1.0 V vs. Ag/AgCl with rotation speed of 1600 rpm. The effect of current/resistance of the cell is not considered (no iR compensation) to any of the obtained data. From the RDE results, electron transfer number, n, was measured using Koutecky-Levich (K-L) relation correlated from the current densities measured. The K-L equations are as follows;

$$\frac{1}{J} = \frac{1}{J_L} + \frac{1}{J_K} = \frac{1}{B\omega^{1/2}} + \frac{1}{J_K}$$

$$B = 0.62nFC_0(D_0)^{2/3}\nu^{-1/6}$$

$$J_K = nFkC_0$$

where J is the measured current density (normalized by the geometric area of the electrode), J_L and J_K are diffusion and kinetic limiting current densities, B is the Levich constant determined by the inverse value of the slope of a straight linear fitting of the measured current densities, ω is the angular rotation velocity of the electrode, F is the Faraday constant (96485 C mol^{-1}) C_0 is the O_2 concentration dissolved in KOH solution (1.2 x 10^{-6} mol cm^{-3}), D_0 is the O_2 diffusion coefficient in electrolyte (1.9 x 10^{-5} cm^2 s^{-1}), and v is the kinetic viscosity of the

KOH electrolyte solution (0.01 cm^2 s^{-1}), respectively. Chronoamperometric test was performed at -0.3 V vs. Ag/AgCl for ORR and 0.7 V vs. Ag/AgCl for OER with constant RDE rotation of 1600 rpm. Recorded Ag/AgCl reference electrode potentials were converted to reversible hydrogen electrode (RHE) potential range using the following relations:

$$E_{RHE} = E_{vs.Ag/AgCl} + 0.197 + 0.059\,pH$$

$$E_{RHE} = E_{vs.Ag/AgCl} + 0.964$$

Consequently, the RHE conversion is defined by the addition of 0.964 V to measured potentials in 0.1 M KOH system.

Supporting Information

Supporting Information is available from the Wiley Online Library or from the author.

Acknowledgements

The authors would like to acknowledge the support by EPSRC (Grant No. EP/K021192/1 and EP/L018330/1) and Keysight Technologies, Inc.

Received: ((will be filled in by the editorial staff))
Revised: ((will be filled in by the editorial staff))
Published online: ((will be filled in by the editorial staff))

References

[1] V. Etacheri, R. Marom, R. Elazari, G. Salitra, D. Aurbach, Energy & Environmental Science 2011, 4, 3243.

[2] Y. Li, H. Dai, Chemical Society Reviews 2014, 43, 5257.

[3] Q. Gao, W. Zhang, Z. Shi, L. Yang, Y. Tang, Advanced Materials 2019, 31.

[4] G. Girishkumar, B. McCloskey, A. C. Luntz, S. Swanson, W. Wilcke, The Journal of Physical Chemistry Letters 2010, 1, 2193; J.-S. Lee, S. Tai Kim, R. Cao, N.-S. Choi, M. Liu, K. T. Lee, J. Cho, Advanced Energy Materials 2011, 1, 34.

[5] Z. Shi, Y. Wang, H. Lin, H. Zhang, M. Shen, S. Xie, Y. Zhang, Q. Gao, Y. Tang, Journal of Materials Chemistry A 2016, 4, 6006.

[6] P. Chen, K. Xu, Z. Fang, Y. Tong, J. Wu, X. Lu, X. Peng, H. Ding, C. Wu, Y. Xie, Angewandte Chemie 2015, 127, 14923; G. Fu, X. Yan, Y. Chen, L. Xu, D. Sun, J.-M. Lee, Y. Tang, Advanced Materials 2017, 30, 1704609; T. Zhao, S. Gadipelli, G. He, J. Ward Matthew, D. Do, P. Zhang, Z. Guo, ChemSusChem 2018, 11, 1295; S. Dou, L. Tao, J. Huo, S. Wang, L. Dai, Energy & Environmental Science 2016, 9, 1320.

[7] Y. Jiao, Y. Zheng, M. Jaroniec, S. Z. Qiao, Journal of the American Chemical Society 2014, 136, 4394; H. Fei, R. Ye, G. Ye, Y. Gong, Z. Peng, X. Fan, E. L. G. Samuel, P. M. Ajayan, J. M. Tour, ACS Nano 2014, 8, 10837.

[8] H. Wang, T. Maiyalagan, X. Wang, ACS Catalysis 2012, 2, 781.

[9] L. Qu, Y. Liu, J.-B. Baek, L. Dai, ACS Nano 2010, 4, 1321; Y. Jia, J. Chen, X. Yao, Materials Chemistry Frontiers 2018, 2, 1250.

[10] J. Liang, Y. Jiao, M. Jaroniec, Z. Qiao Shi, Angewandte Chemie International Edition 2012, 51, 11496.

[11] R. Li, Z. Wei, X. Gou, ACS Catalysis 2015, 5, 4133; S. Yang, L. Zhi, K. Tang, X. Feng, J. Maier, K. Müllen, Advanced Functional Materials 2012, 22, 3634.

[12] Y. Dong, H. Pang, H. B. Yang, C. Guo, J. Shao, Y. Chi, C. M. Li, T. Yu, Angew Chem Int Ed Engl 2013, 52, 7800; S. Zhu, Q. Meng, L. Wang, J. Zhang, Y. Song, H. Jin, K. Zhang, H. Sun, H. Wang, B. Yang, Angew Chem Int Ed Engl 2013, 52, 3953.

[13] D. Pan, J. Zhang, Z. Li, M. Wu, Adv Mater 2010, 22, 734.

[14] B. C. M. Martindale, G. A. M. Hutton, C. A. Caputo, S. Prantl, R. Godin, J. R. Durrant, E. Reisner, Angew Chem Int Ed Engl 2017, 56, 6459.

[15] B. De, N. Karak, Journal of Materials Chemistry A 2017, 5, 1826; Y. Jia, L. Zhang, A. Du, G. Gao, J. Chen, X. Yan, C. L. Brown, X. Yao, Advanced Materials 2016, 28, 9532.

[16] S. N. Baker, G. A. Baker, Angew Chem Int Ed Engl 2010, 49, 6726; C. Tang, Q. Zhang, Advanced Materials 2017, 29, 1604103.

[17] X. Zhou, Z. Tian, J. Li, H. Ruan, Y. Ma, Z. Yang, Y. Qu, Nanoscale 2014, 6, 2603; C. Hu, C. Yu, M. Li, X. Wang, Q. Dong, G. Wang, J. Qiu, Chemical Communications 2015, 51, 3419; W.-J. Niu, R.-H. Zhu, H. Yan, H.-B. Zeng, S. Cosnier, X.-J. Zhang, D. Shan, Carbon 2016, 109, 402; Q. Li, S. Zhang, L. Dai, L.-s. Li, Journal of the American Chemical Society 2012, 134, 18932; S. Bhattacharyya, B. Konkena, K. Jayaramulu, W. Schuhmann, T. K. Maji, Journal of Materials Chemistry A 2017, 5, 13573.

[18] D. C. Marcano, D. V. Kosynkin, J. M. Berlin, A. Sinitskii, Z. Sun, A. Slesarev, L. B. Alemany, W. Lu, J. M. Tour, ACS Nano 2010, 4, 4806.

[19] A. M. Dimiev, J. M. Tour, ACS Nano 2014, 8, 3060.

[20] J. I. Paredes, S. Villar-Rodil, A. Martínez-Alonso, J. M. D. Tascón, Langmuir 2008, 24, 10560.

[21] V. H. Luan, H. N. Tien, L. T. Hoa, N. T. M. Hien, E.-S. Oh, J. Chung, E. J. Kim, W. M. Choi, B.-S. Kong, S. H. Hur, Journal of Materials Chemistry A 2013, 1, 208.

[22] K. Habiba, V. I. Makarov, J. Avalos, M. J. Guinel, B. R. Weiner, G. Morell, Carbon N Y 2013, 64, 341; D. K. Pandey, T. F. Chung, G. Prakash, R. Piner, Y. P. Chen, R. Reifenberger, Surface Science 2011, 605, 1669; S. Yang, J. Sun, C. Zhu, P. He, Z. Peng, G. Ding, Analyst 2016, 141, 1052.

[23] A. C. Ferrari, Solid State Communications 2007, 143, 47; A. C. Ferrari, D. M. Basko, Nature Nanotechnology 2013, 8, 235.

[24] M. Xue, L. Zhang, Z. Zhan, M. Zou, Y. Huang, S. Zhao, Talanta 2016, 150, 324.

[25] Z.-H. Sheng, L. Shao, J.-J. Chen, W.-J. Bao, F.-B. Wang, X.-H. Xia, ACS Nano 2011, 5, 4350.

[26] Y. Wang, S. H. Kim, L. Feng, Anal Chim Acta 2015, 890, 134.

[27] Y. Zhang, Y. Wang, X. Feng, F. Zhang, Y. Yang, X. Liu, Applied Surface Science 2016, 387, 1236.

[28] Z. Luo, D. Yang, G. Qi, J. Shang, H. Yang, Y. Wang, L. Yuwen, T. Yu, W. Huang, L. Wang, J. Mater. Chem. A 2014, 2, 20605.

[29] T.-F. Yeh, S.-J. Chen, H. Teng, Nano Energy 2015, 12, 476.

[30] G. Zhou, E. Paek, G. S. Hwang, A. Manthiram, Nat Commun 2015, 6, 7760.

[31] H. Ding, J. S. Wei, H. M. Xiong, Nanoscale 2014, 6, 13817; S. Kundu, R. M. Yadav, T. N. Narayanan, M. V. Shelke, R. Vajtai, P. M. Ajayan, V. K. Pillai, Nanoscale 2015, 7, 11515; Y.-W. Zeng, D.-K. Ma, W. Wang, J.-J. Chen, L. Zhou, Y.-Z. Zheng, K. Yu, S.-M. Huang, Applied Surface Science 2015, 342, 136; Y. Zhang, J. He, Phys Chem Chem Phys 2015, 17, 20154.

[32] B. Ryan, C. Luiz Gustavo, N. Lukas, Journal of Physics: Condensed Matter 2015, 27, 083002; F. Tuinstra, J. L. Koenig, The Journal of Chemical Physics 1970, 53, 1126.

[33] D. Geng, S. Yang, Y. Zhang, J. Yang, J. Liu, R. Li, T.-K. Sham, X. Sun, S. Ye, S. Knights, Applied Surface Science 2011, 257, 9193.

[34] L.-H. Kao, T.-C. Hsu, Materials Letters 2008, 62, 695; Z. Pei, H. Li, Y. Huang, Q. Xue, Y. Huang, M. Zhu, Z. Wang, C. Zhi, Energy & Environmental Science 2017, 10, 742.

[35] R. Arrigo, M. Havecker, R. Schlogl, D. S. Su, Chem Commun (Camb) 2008, 4891.

[36] Z. J. Li, B. C. Yang, S. R. Zhang, C. M. Zhao, Applied Surface Science 2012, 258, 3726.

[37] Q. Dong, S. Santhanagopalan, R. E. White, Journal of The Electrochemical Society 2007, 154.

[38] Y. Liu, H. Wang, D. Lin, J. Zhao, C. Liu, J. Xie, Y. Cui, Nano Research 2017, 10, 1213.

[39] O. Marciano, S. Gonen, N. Levy, E. Teblum, R. Yemini, G. D. Nessim, S. Ruthstein, L. Elbaz, Langmuir 2016, 32, 11672.

[40] J.-M. You, M. S. Ahmed, H. S. Han, J. e. Choe, Z. Üstündağ, S. Jeon, Journal of Power Sources 2015, 275, 73.

[41] Z. Yang, Z. Yao, G. Li, G. Fang, H. Nie, Z. Liu, X. Zhou, X. a. Chen, S. Huang, ACS Nano 2012, 6, 205.

[42] A. M. El-Sawy, I. M. Mosa, D. Su, C. J. Guild, S. Khalid, R. Joesten, J. F. Rusling, S. L. Suib, Advanced Energy Materials 2016, 6; H. B. Yang, J. Miao, S. Hung, J. Chen, H. B. Tao, X. Wang, L. Zhang, R. Chen, J. Gao, H. M. Chen, L. Dai, B. Liu, Science Advances 2016, 2.

[43] Z. Lu, L. Qian, Y. Tian, Y. Li, X. Sun, X. Duan, Chemical Communications 2016, 52, 908.

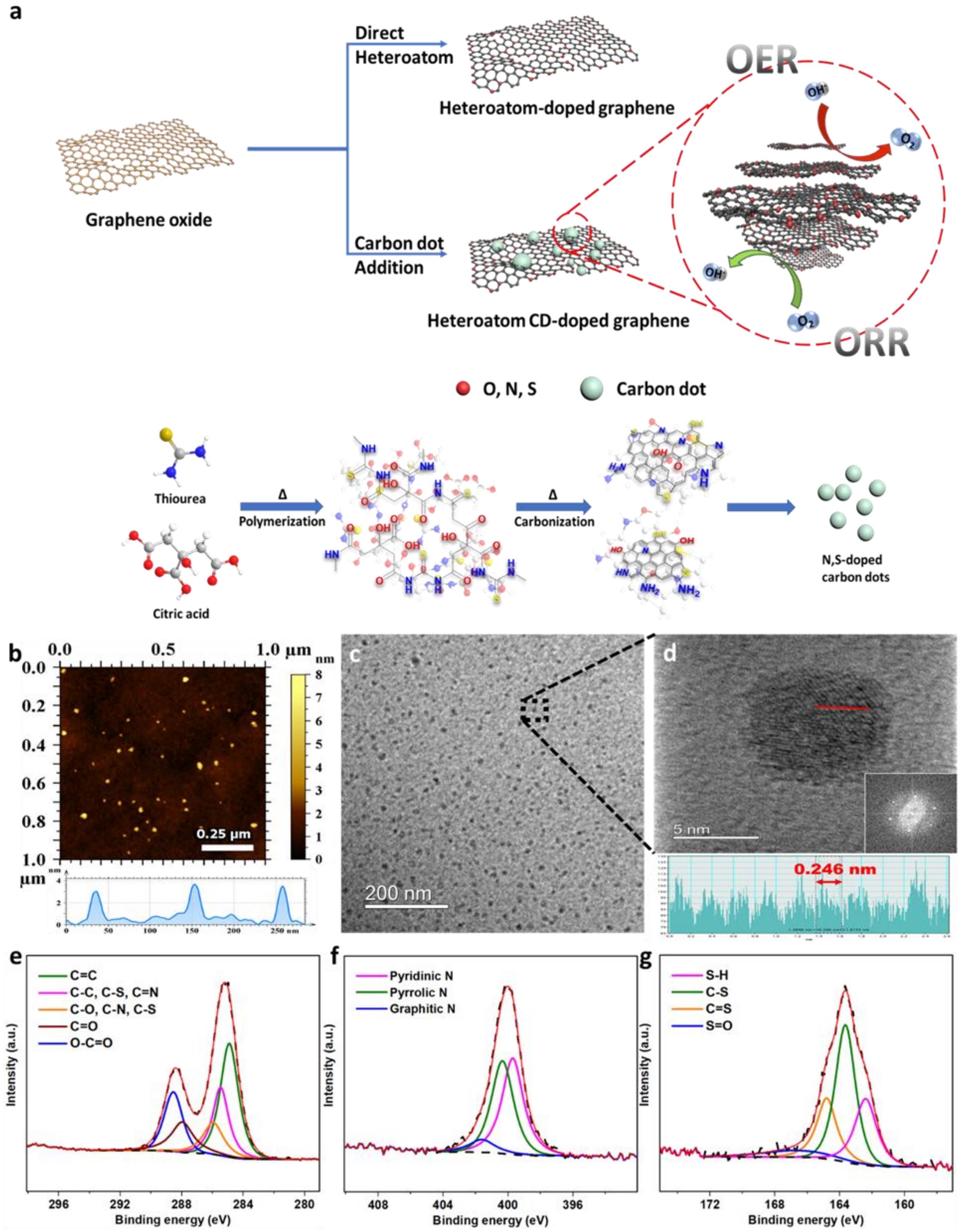

Figure 1. (a) Schematic illustration of the carbon dots embedded porous carbon (CD@gf) fabrication where red spheres represent dopants (either O, N, and S), and light green spheres represent carbon dots (of any kind). (b) AFM topology of well-dispersed NS-CD with height

profile. TEM images of NS-CD in (c) low, and (d) high magnification with height profile; the inset is the corresponding reduced-FFT image. High resolution XPS spectra of NS-CD; (e) C 1s, (f) N 1s, and (g) S 2p.

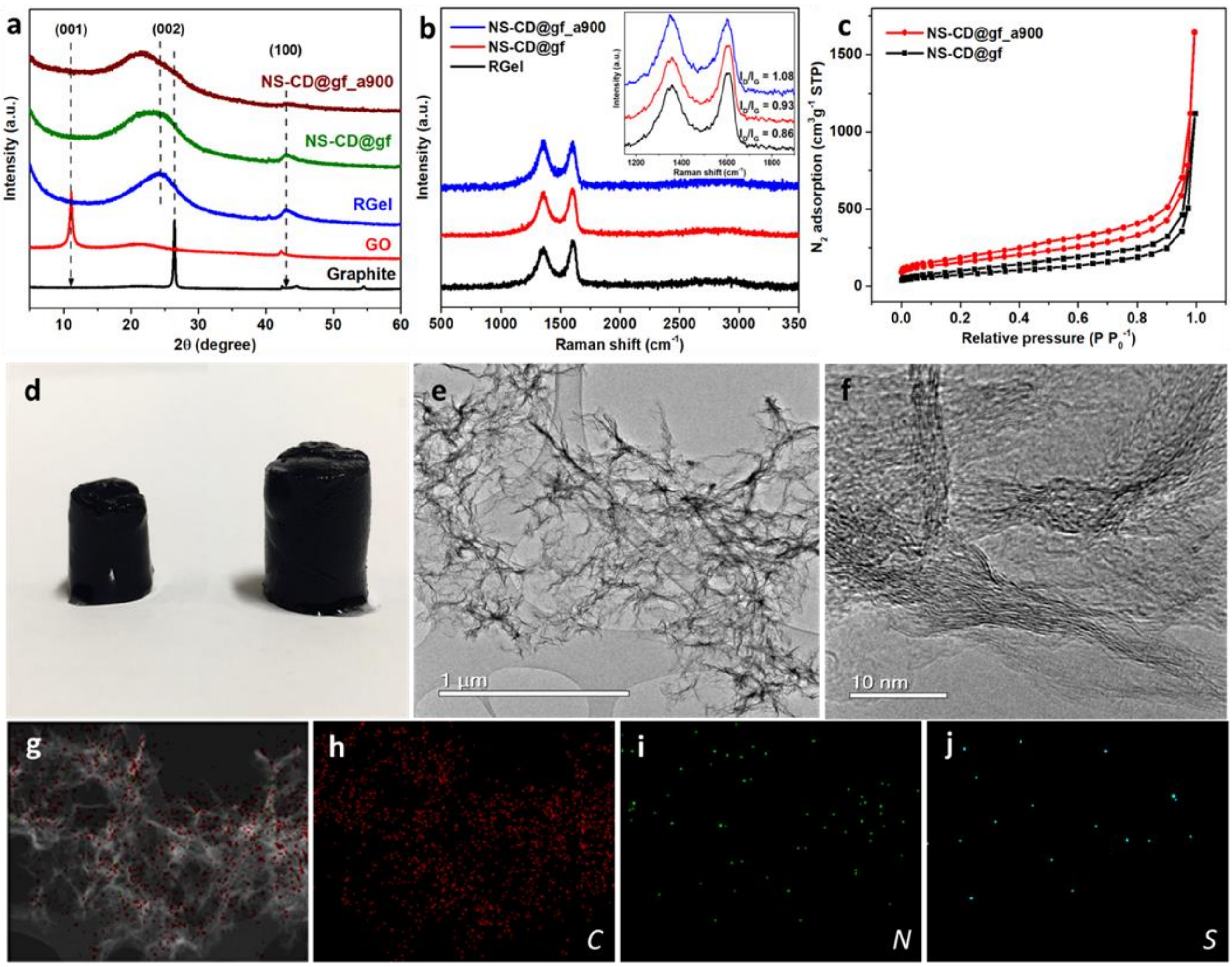

Figure 2. (a) XRD patterns of graphite, GO, RGel, NS-CD@gf, and NS-CD@gf_a900. (b) Raman spectra of RGel, NS-CD@gf, and NS-CD@gf_a900; the inset is the close-up of D and G band with relative I_D/I_G ratio. (c) N_2 adsorption-desorption isotherm of NS-CD@gf, and NS-CD@gf_a900. (d) Photo of hydrothermally prepared RGel (left), and NS-CD@gf (right). TEM images of NS-CD@gf_a900 in (e) low, and (f) high magnification showing highly porous carbon. (g-j) EDS mapping of the above TEM image showing different elements (C, N, S) of the NS-CD@gf_a900 framework.

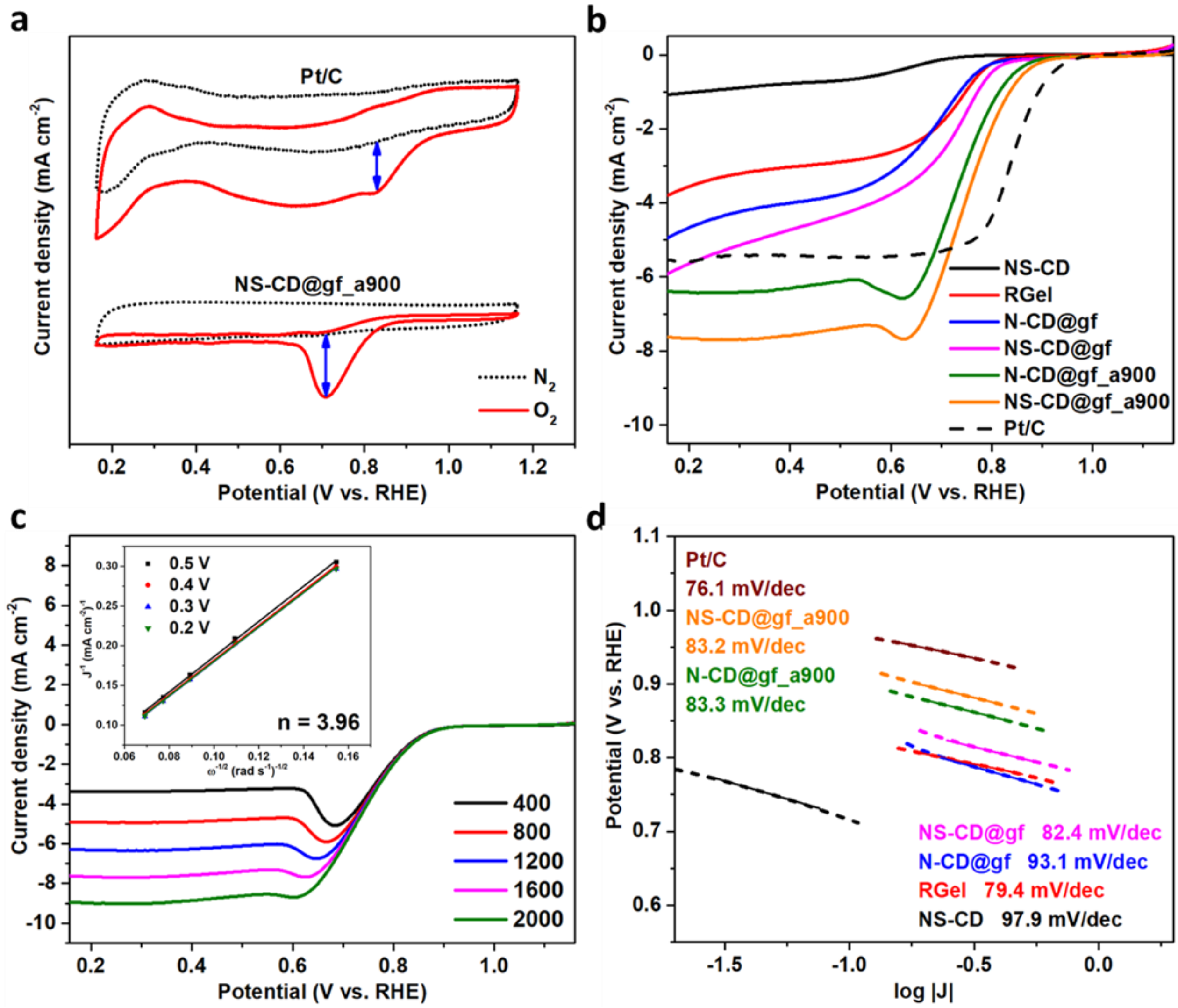

Figure 3. (a) CV curves of NS-CD@gf_a900 and Pt/C obtained in N_2/O_2 saturated 0.1 M KOH with the scan rate of 10 mV s^{-1}. (b) Combined LSV curves for ORR of all CD-containing samples in O_2 saturated 0.1 M KOH at rotation speed of 1600 rpm. (c) LSV curves of the NS-CD@gf_a900 recorded at different rotation speeds (rpm); the inset is the K-L plots calculated at the potential range 0.2-0.5 V vs. RHE at different rotation speeds. (d) ORR Tafel plots of all samples in 0.1 M KOH solution at 1600 rpm.

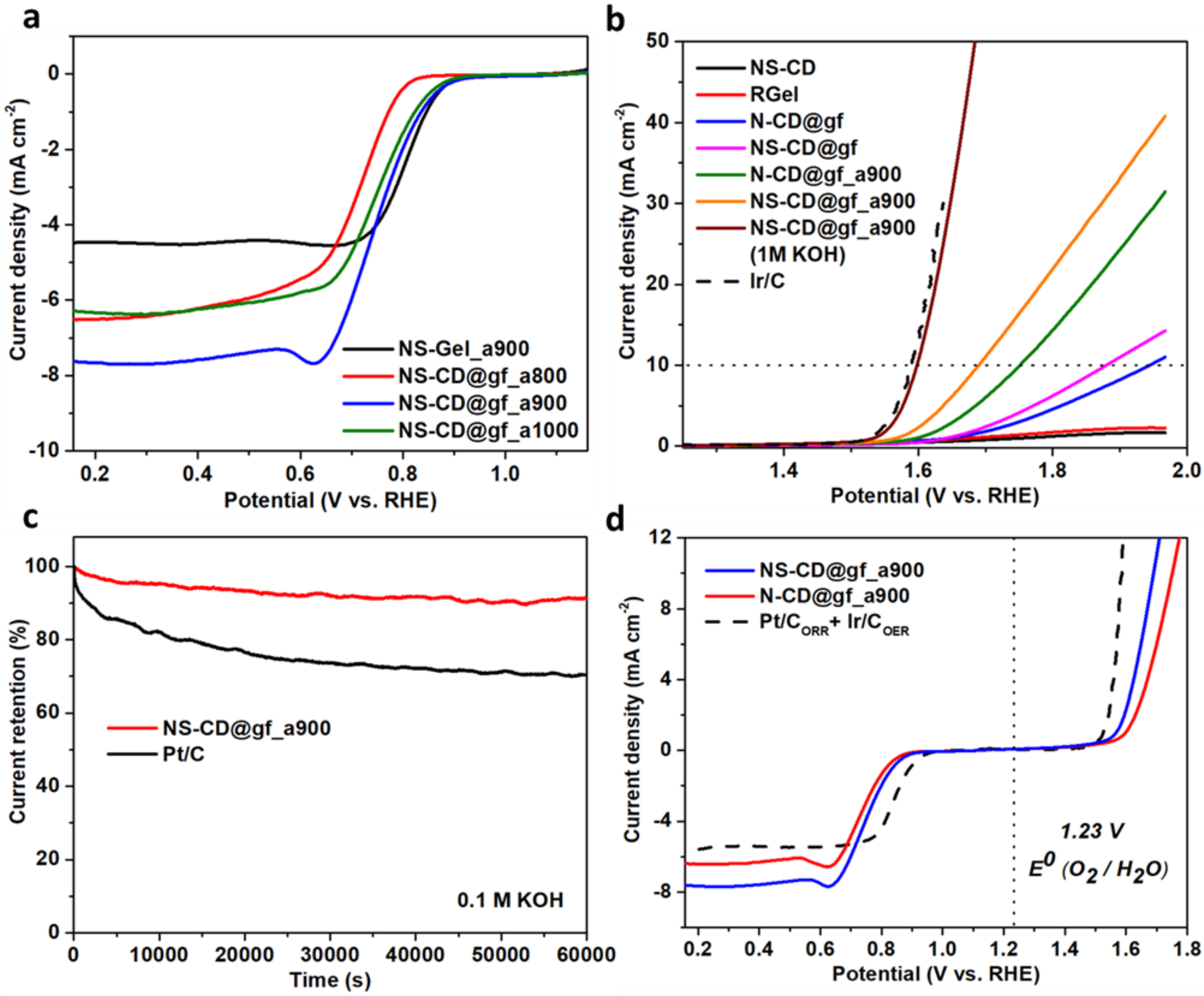

Figure 4. (a) ORR LSV curves of NS-Gel_a900, and temperature-controlled CD samples; NS-CD@gf_a800, NS-CD@gf_a900, and NS-CD@gf_a1000 in 0.1 M KOH with rotation of 1600 rpm. (b) Combined LSV curves for OER of all CD-containing samples and Ir/C in O_2 saturated 0.1 M KOH at rotation speed of 1600 rpm; a LSV curve of NS-CD@gf_a900 in 1 M KOH solution. (c) Chronoamperometric stability plot (current vs. time) of NS-CD@gf_a900 and Pt/C in 0.1 M KOH solution in the ORR region with fixed rotation at 1600 rpm. (d) Combined LSV curves of N-CD@gf_a900, NS-CD@gf_a900, and conventional catalysts displaying the bifunctionality in ORR/OER region. Ir/C activity obtained from literature.[43]

Heteroatom-doped carbon dots embedded porous graphene provide enriched active sites for bi-functional oxygen electrocatalysis. Controlling the size and functional groups of carbon, performances are comparable to noble-metal containing species with good stability. This appoints the utilization of a new class of non-metal electrocatalyst.

Keyword: carbon dots, bi-functional, oxygen electrocatalyst, metal-free, heteroatoms

J. Shin, J. Guo, T. Zhao, Z. X. Guo*

Functionalized Carbon Dots on Graphene as Outstanding Non-Metal Bi-Functional Oxygen Electrocatalyst

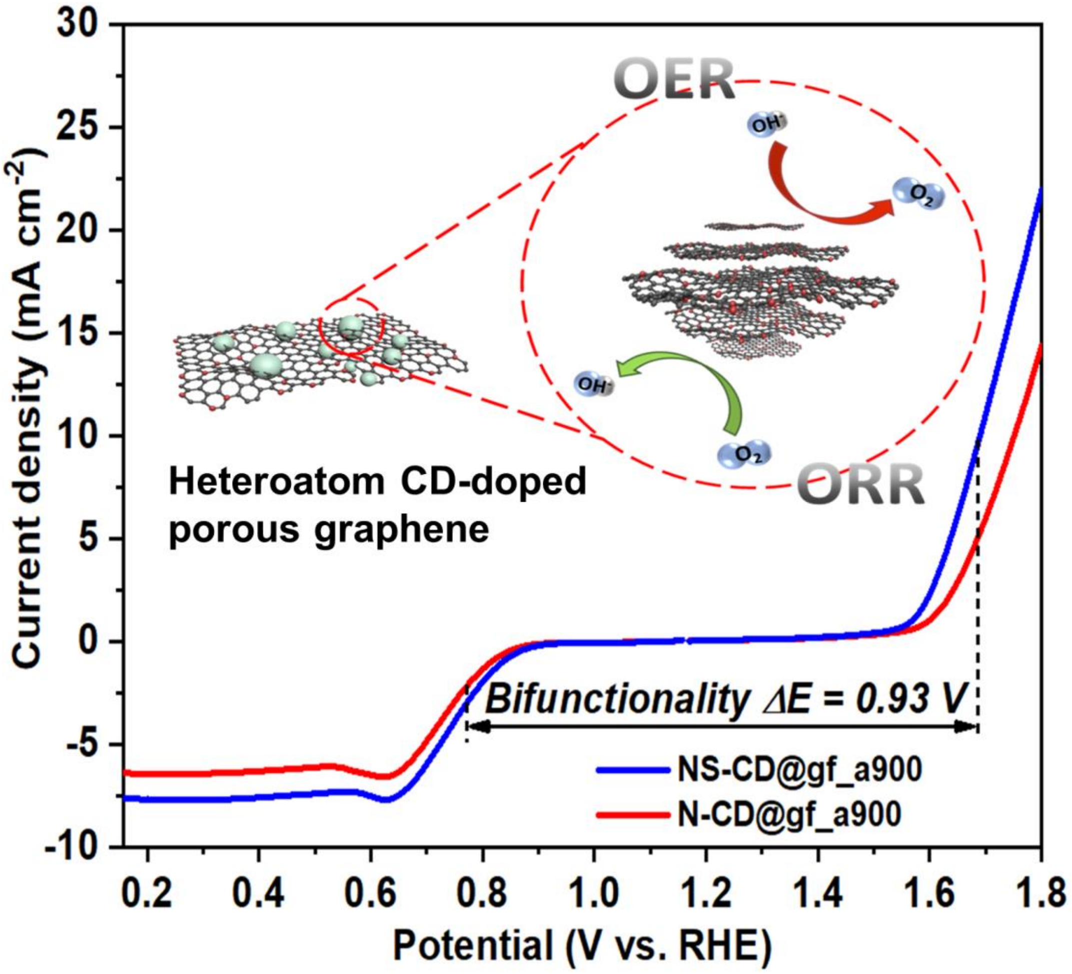

((Supporting Information can be included here using this template))

Supporting Information

Functionalized Carbon Dots on Graphene as Outstanding Non-Metal Bi-Functional Oxygen Electrocatalyst

*Juhun Shin, Jian Guo, Tingting Zhao, and Zhengxiao Guo**

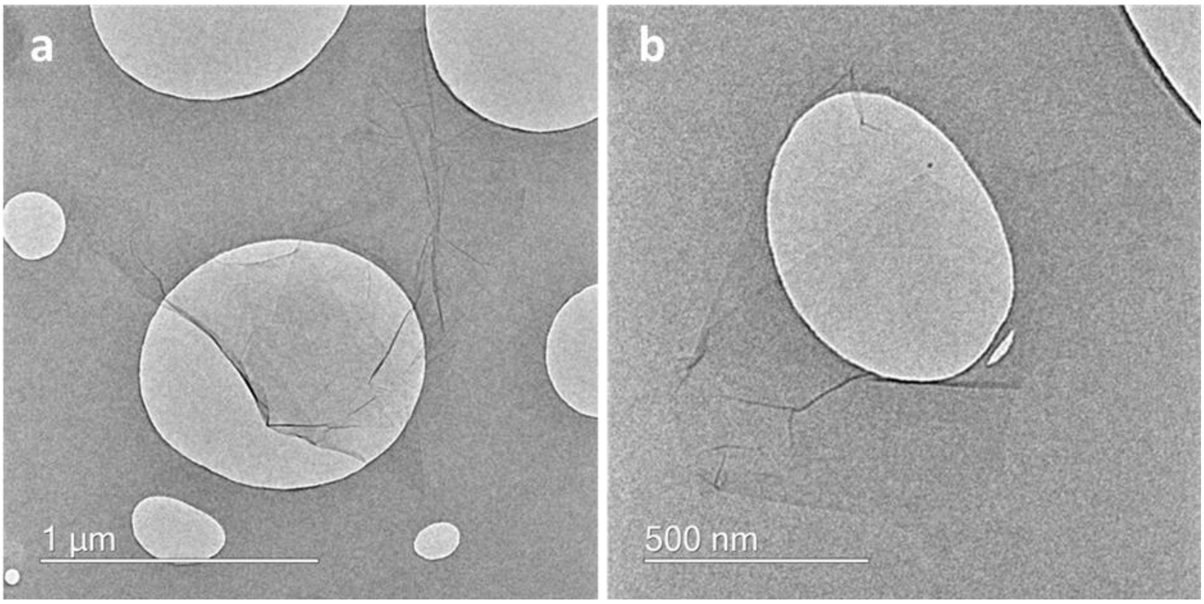

Figure S1. TEM images of GO with high degree of exfoliation shown by the contrast of the sheets compared to the grid.

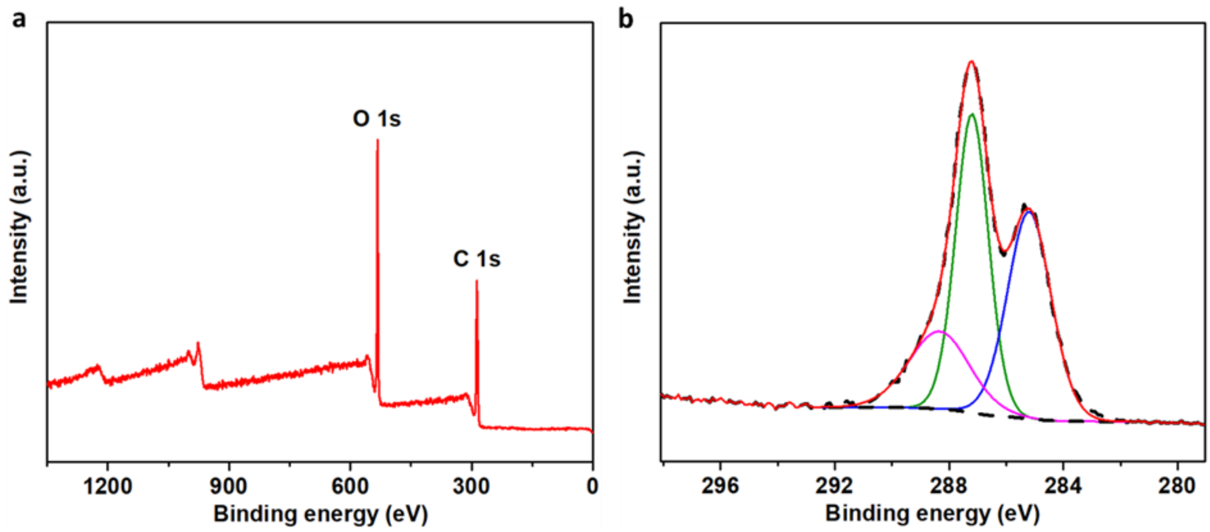

Figure S2. (a) XPS survey spectrum of GO with C/O ratio of 1.96. (b) C 1s spectrum of GO with peaks at 285.1, 287.2, and 288.4 eV corresponding to C-C/C=C, C-O, and C=O bonds.

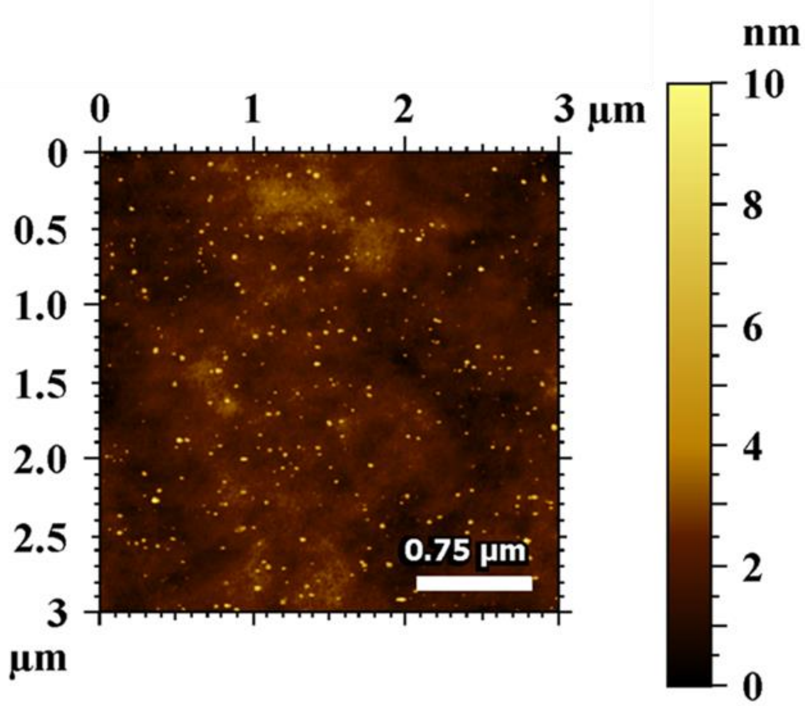

Figure S3. AFM topology of NS-CD at low magnification.

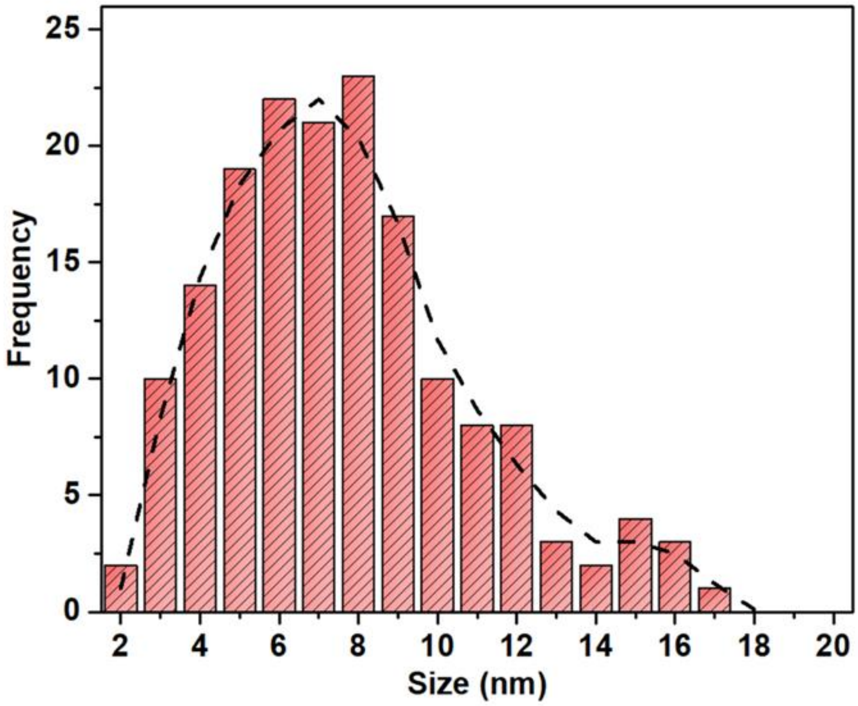

Figure S4. TEM particle size distribution of NS-CD; average particle size is 8.5 nm.

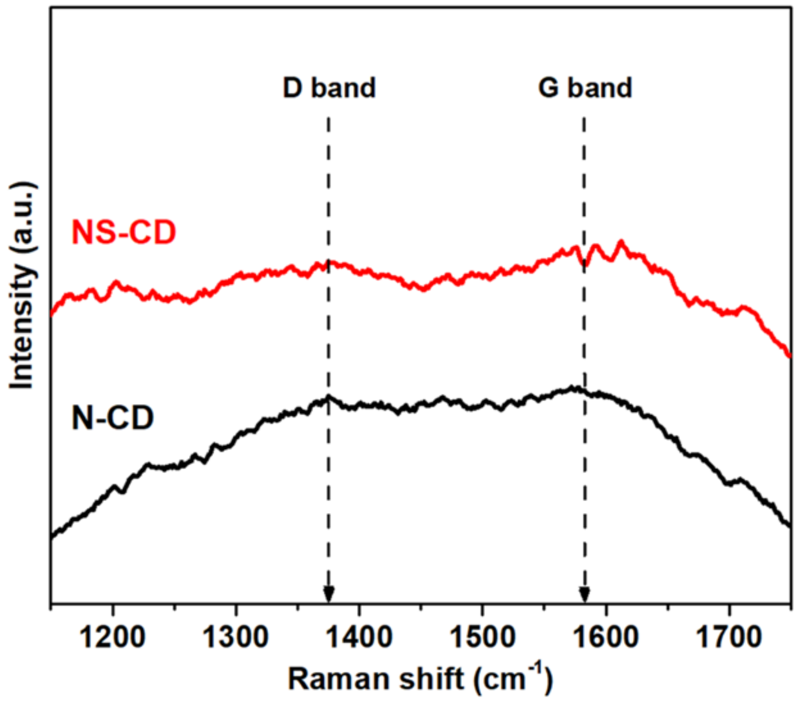

Figure S5. Raman spectra of N-CD and NS-CD between 1200-1700 cm-1 region with weak D and G band signals.

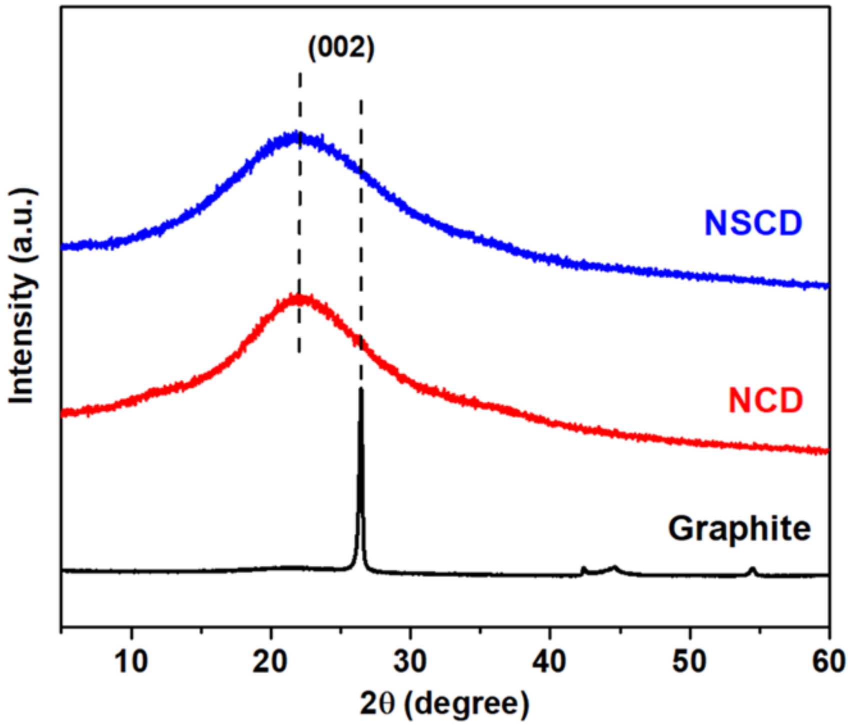

Figure S6. XRD patterns of N-CD and NS-CD against graphite reference.

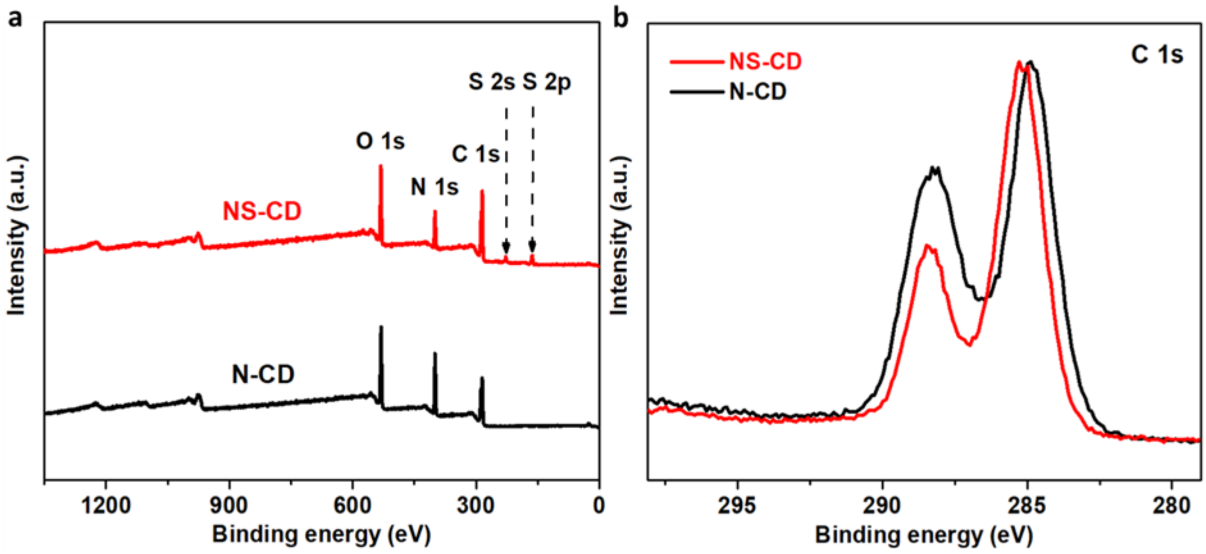

Figure S7. (a) XPS survey spectra of N-CD and NS-CD with peaks corresponding to energies of elements present. (b) Overlap of C 1s spectra of N-CD and NS-CD revealing the energy shift.

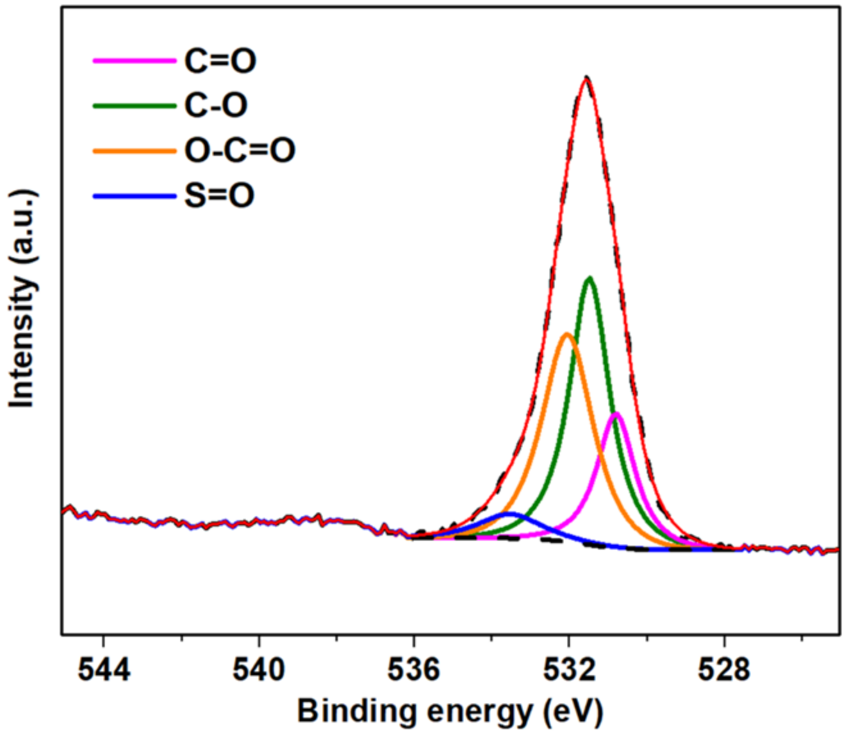

Figure S8. O 1s spectrum of NS-CD

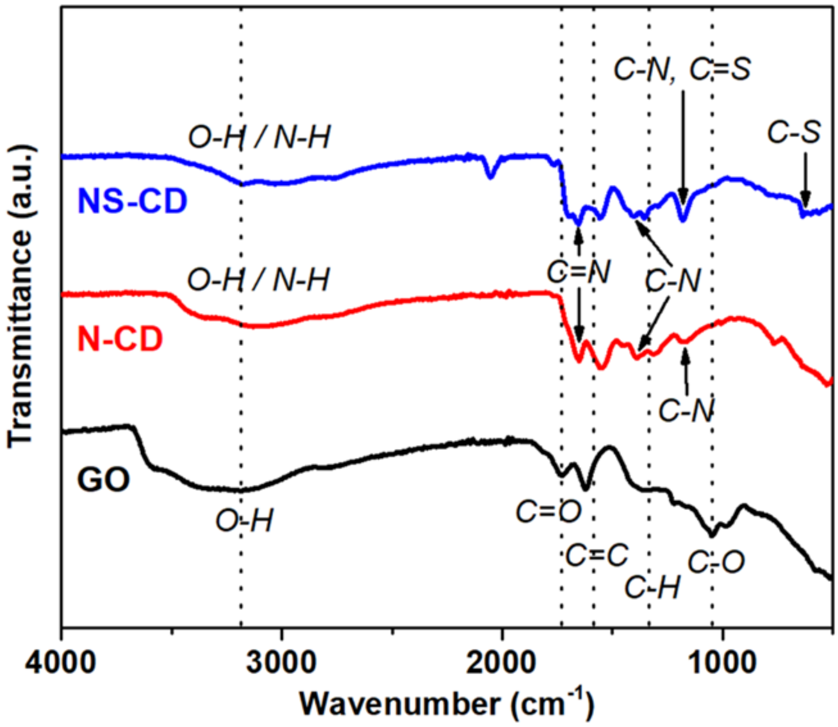

Figure S9. ATR of GO, N-CD, and NS-CD displaying various chemical environments.

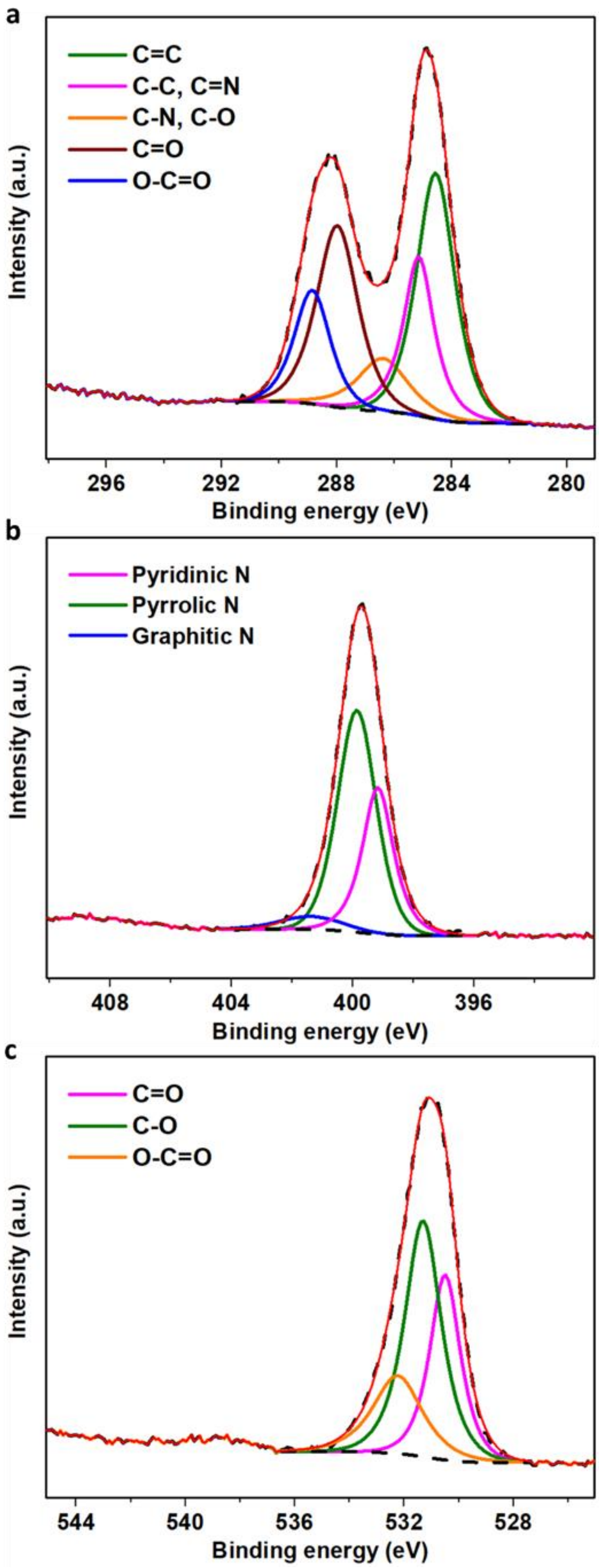

Figure S10. High resolution XPS spectro of N-CD; (a) C 1s, (b) N 1s, and (c) O 1s.

Table S1. Quantification of elements obtained from XPS for N-CD and NS-CD samples.

Sample	C (at. %)	N (at. %)	S (at. %)	O (at. %)	Pyrid N (%)	Pyrrol N (%)	G-N (%)
N-CD	62.73	10.38	–	26.88	34.39	59.98	5.64
NS-CD	65.86	8.91	3.37	21.87	47.13	46.56	6.32

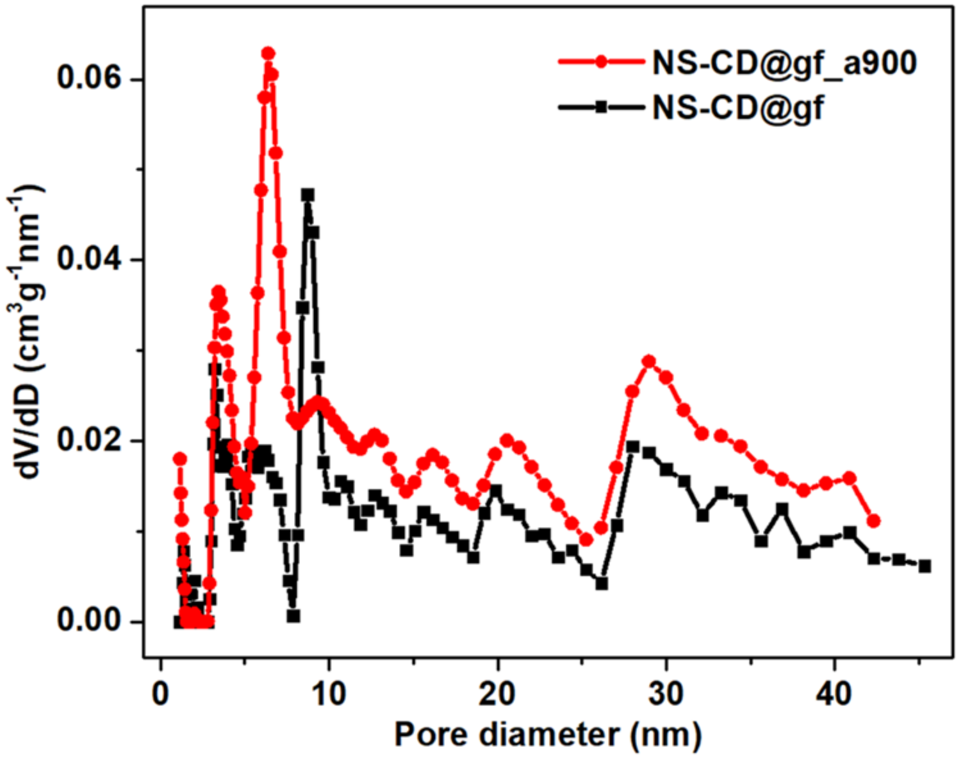

Figure S11. BET pore size distribution curves of NS-CD@gf and NS-CD@gf_a900 using QSDFT and BJH methods

Table S2. Total BET surface area and pore volume for all samples.

Sample	**BET surface area (m^2 g^{-1})**	**Total pore volume (cm^3 g^{-1})**
RGel	345.02	1.82
N-CD@gf	255.88	1.76
NS-CD@gf	264.66	1.73
N-CD@gf_a900	550.20	3.19
NS-CD@gf_a900	559.59	2.54

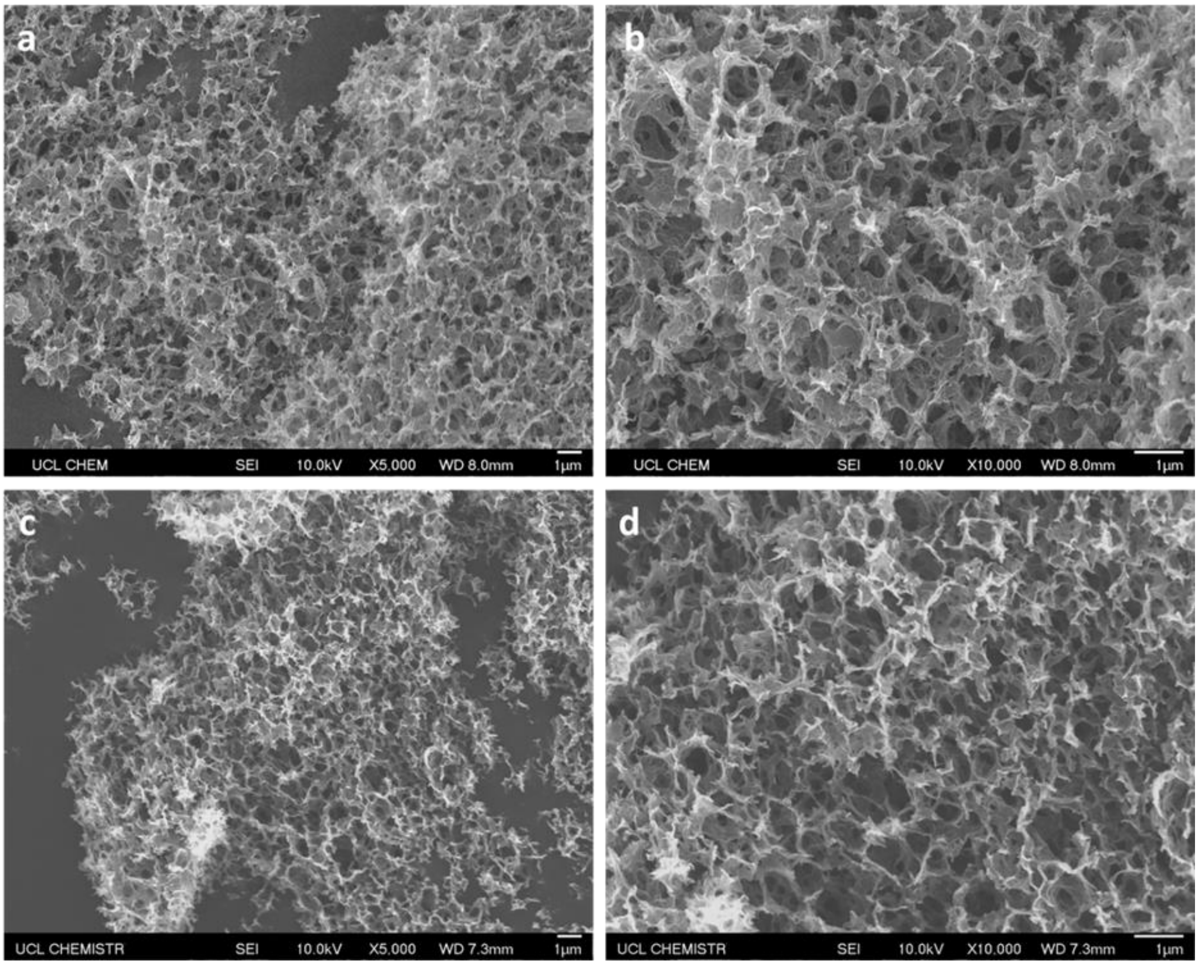

Figure S12. SEM images of N-CD@gf_a900 in (a) low, (b) high, and NS-CD@gf_a900 in (c) low, and (d) high magnification.

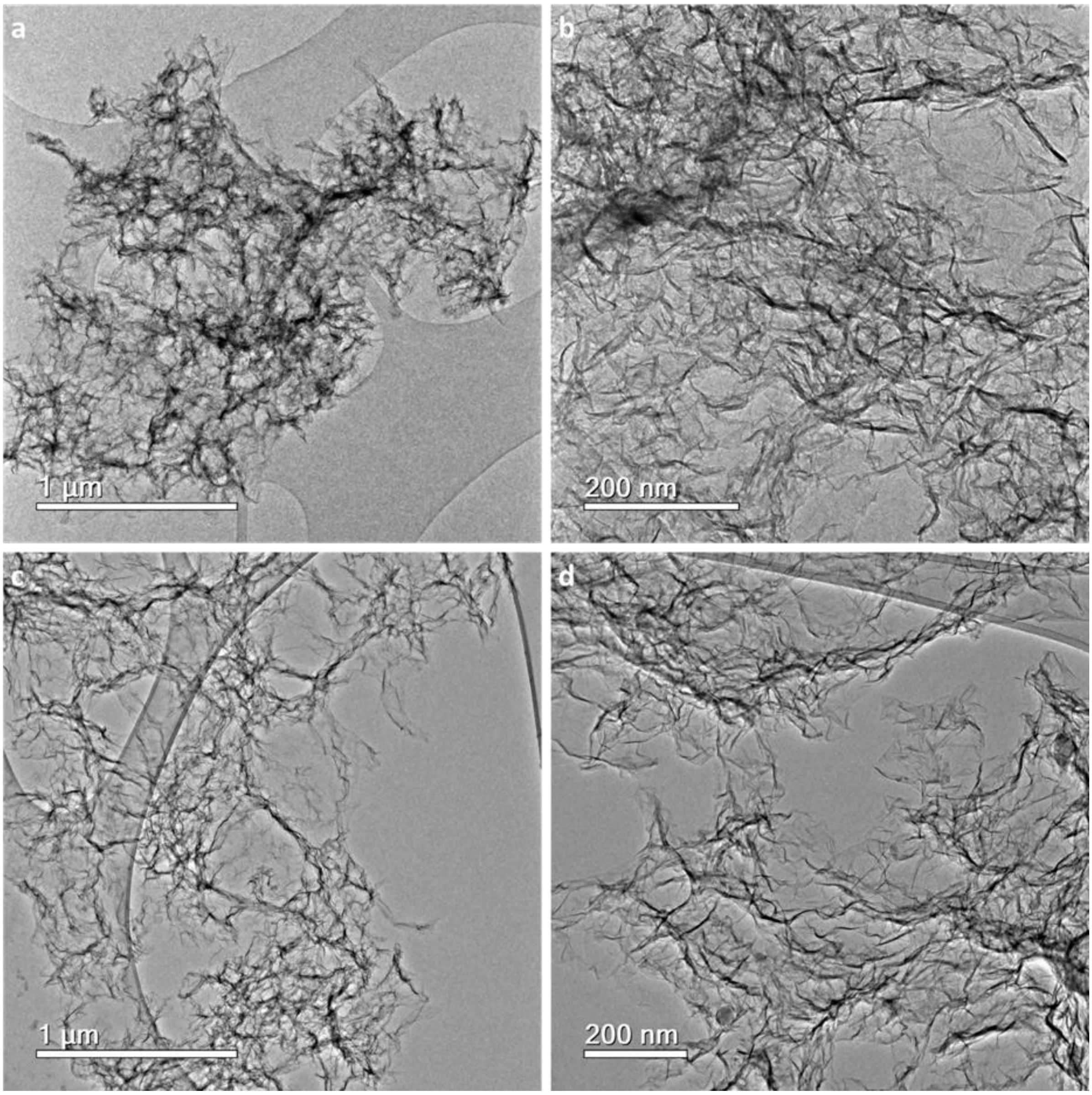

Figure S13. TEM images N-CD@gf_a900 in (a) low, (b) high magnification, and NS-CD@gf_a900 in (c) low, and (d) high magnification.

Table S3. Quantification of elements obtained from XPS for N-CD@gf, N-CD@gf_a900, NS-CD@gf, and NS-CD@gf_a900 samples.

Sample	**C (at. %)**	**N (at. %)**	**S (at. %)**	**O (at. %)**
N-CD@gf	83.7	1.59	–	14.71
N-CD@gf_a900	94.9	0.98	–	4.12
NS-CD@gf	87.41	5.24	0.70	6.65
NS-CD@gf_a900	95.37	1.36	0.41	2.86

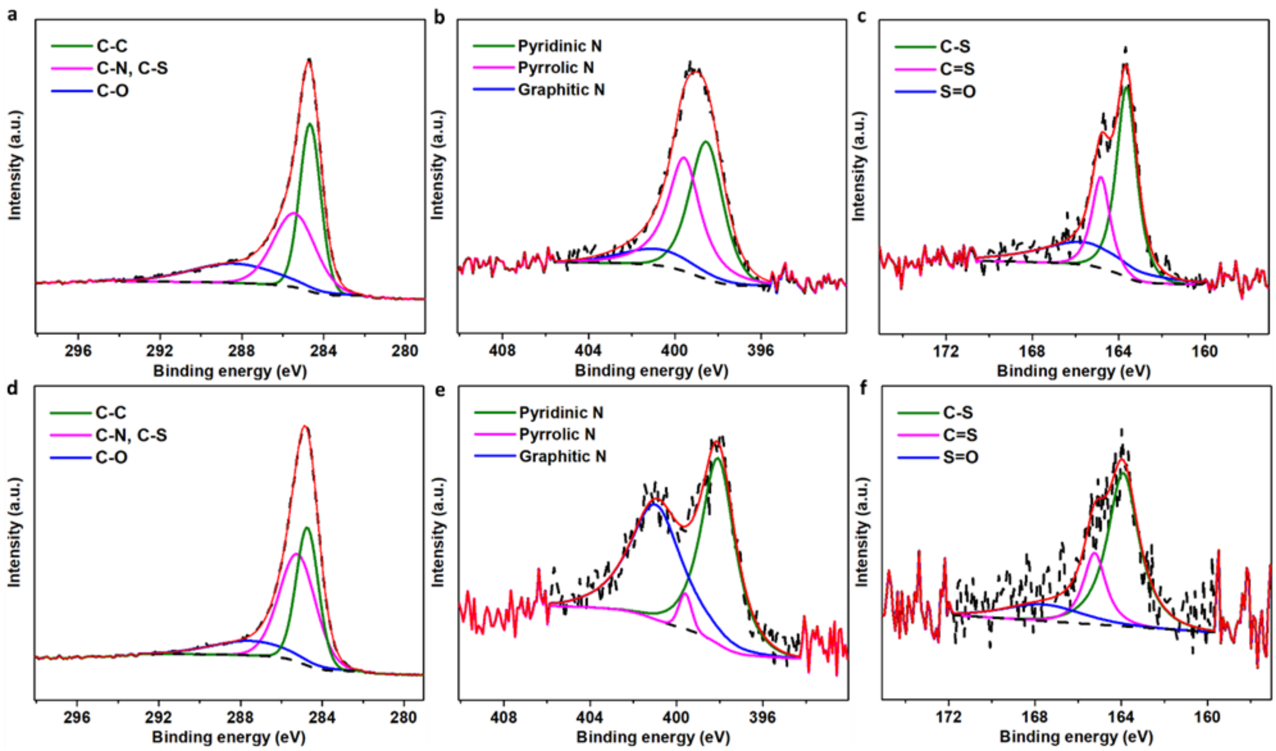

Figure S14. High resolution XPS spectra of NS-CD@gf (a-c); (a) C 1s, (b) N 1s, and (c) S 2p.

Elemental XPS spectra of NS-CD@gf_a900 (d-f); (d) C 1s, (e) N 1s, and (f) S 2p.

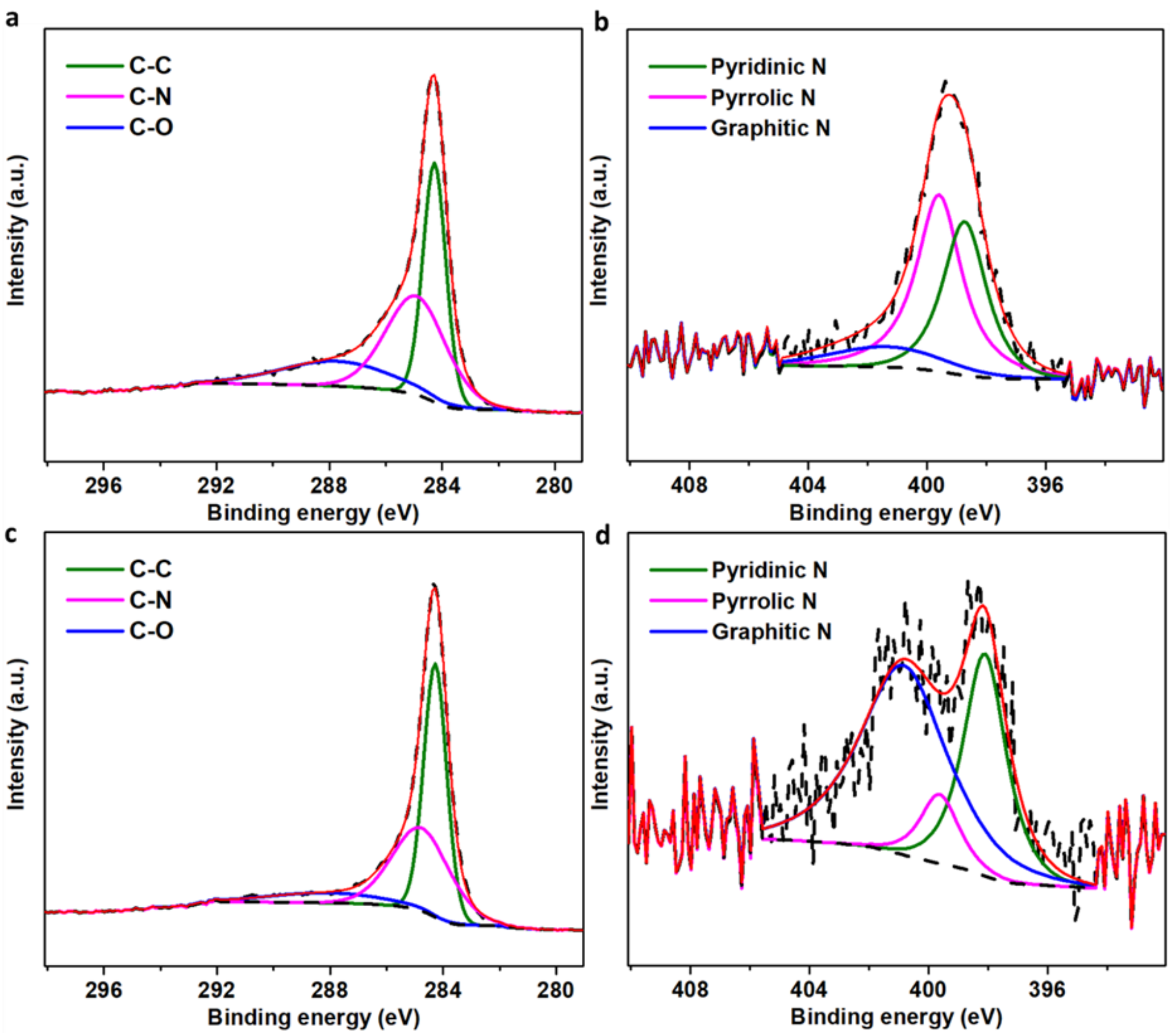

Figure S15. High resolution XPS spectra of N-CD@gf showing (a) C 1s, (b) N 1s, and of N-CD@gf_a900 displaying (c) C 1s, and (d) N 1s.

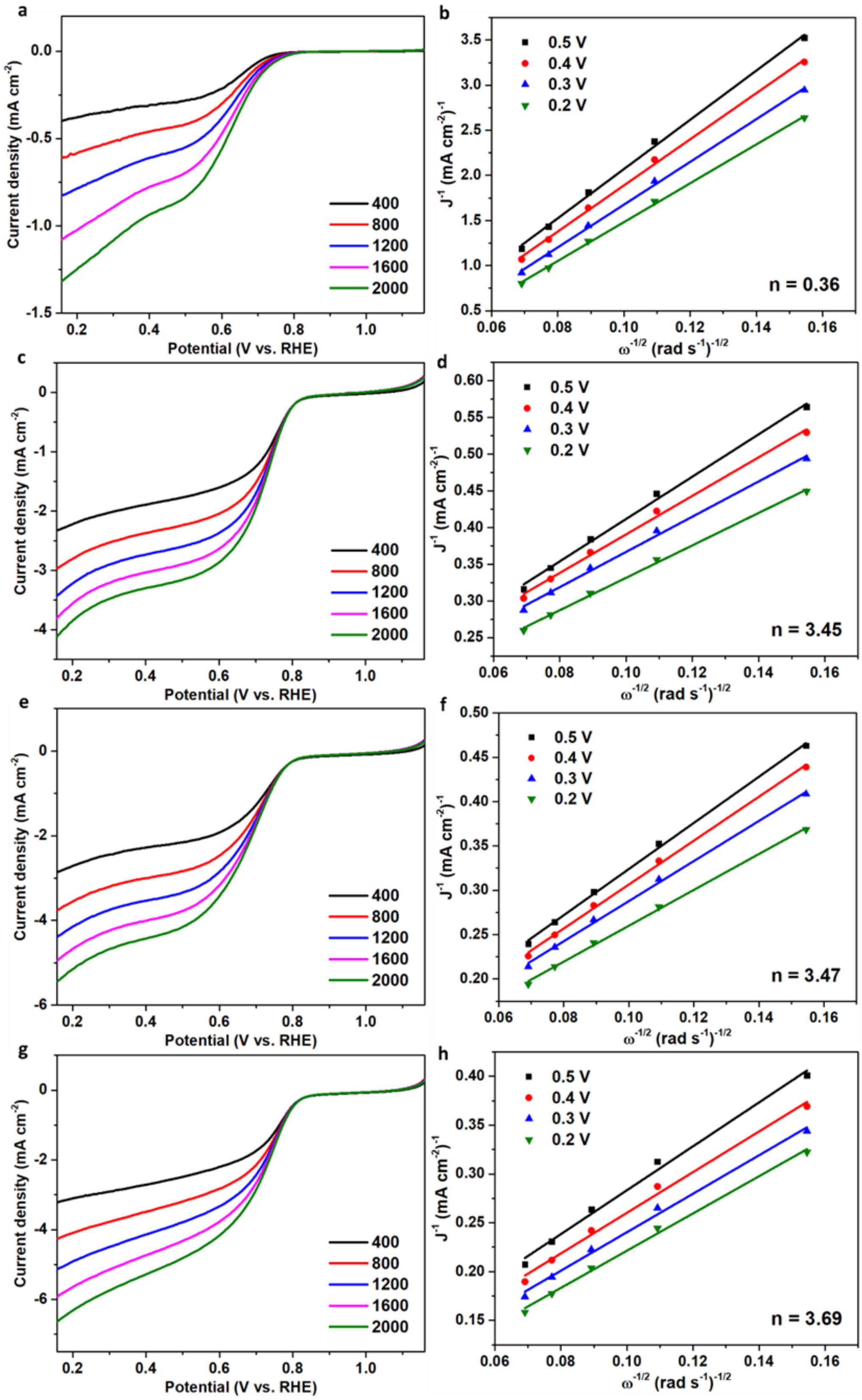

Figure S16. LSV curves at different rotations and corresponding K-L plots for (a-b) NS-CD, (c-d) RGel, (e-f) N-CD@gf, and (g-h) NS-CD@gf.

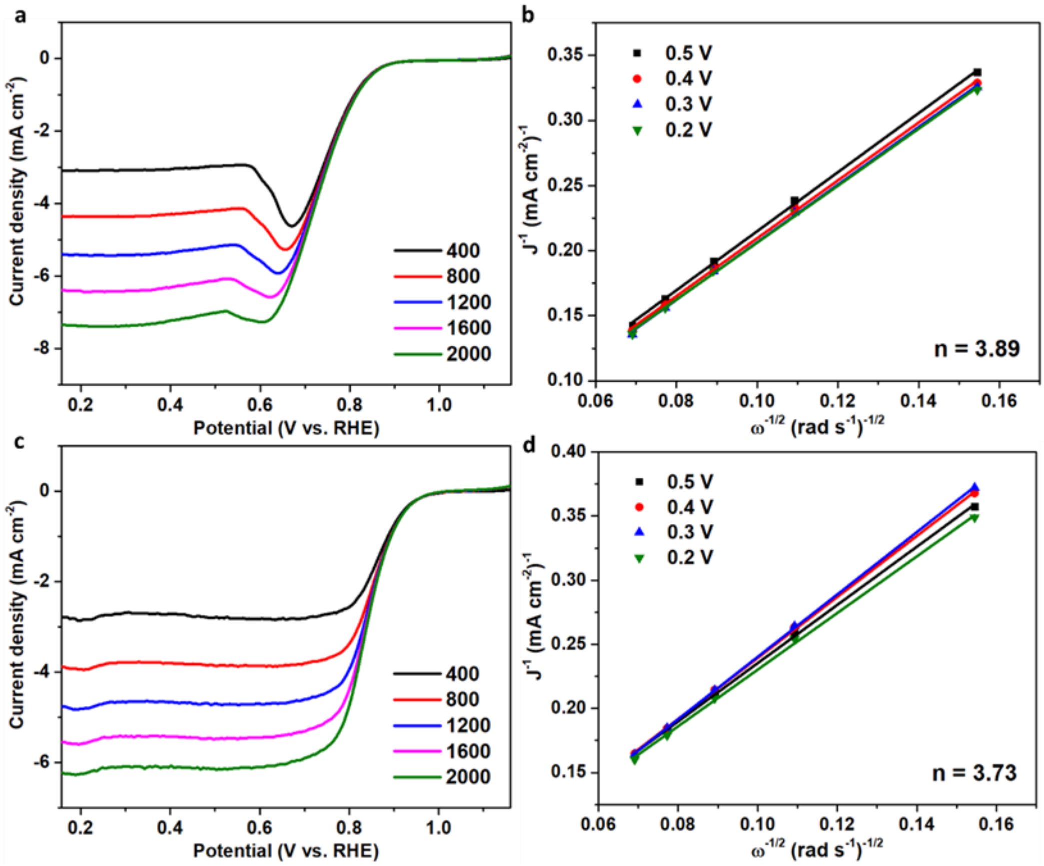

Figure S17. LSV curves and corresponding K-L plots for (a-b) N-CD@gf_a900, and (c-d) Pt/C.

Table S4. Quantification of elements obtained from XPS for temperature controlled samples.

Sample	C (at. %)	N (at. %)	S (at. %)	O (at. %)	Pyrid N (%)	Pyrrol N (%)	G-N (%)
NS-CD@gf_a800	92.51	2.07	0.74	4.68	61.59	8.76	29.65
NS-CD@gf_a900	95.37	1.36	0.41	2.86	33.66	5.89	60.45
NS-CD@gf_a1000	96.18	1.19	0.28	2.35	26.19	7.55	66.26

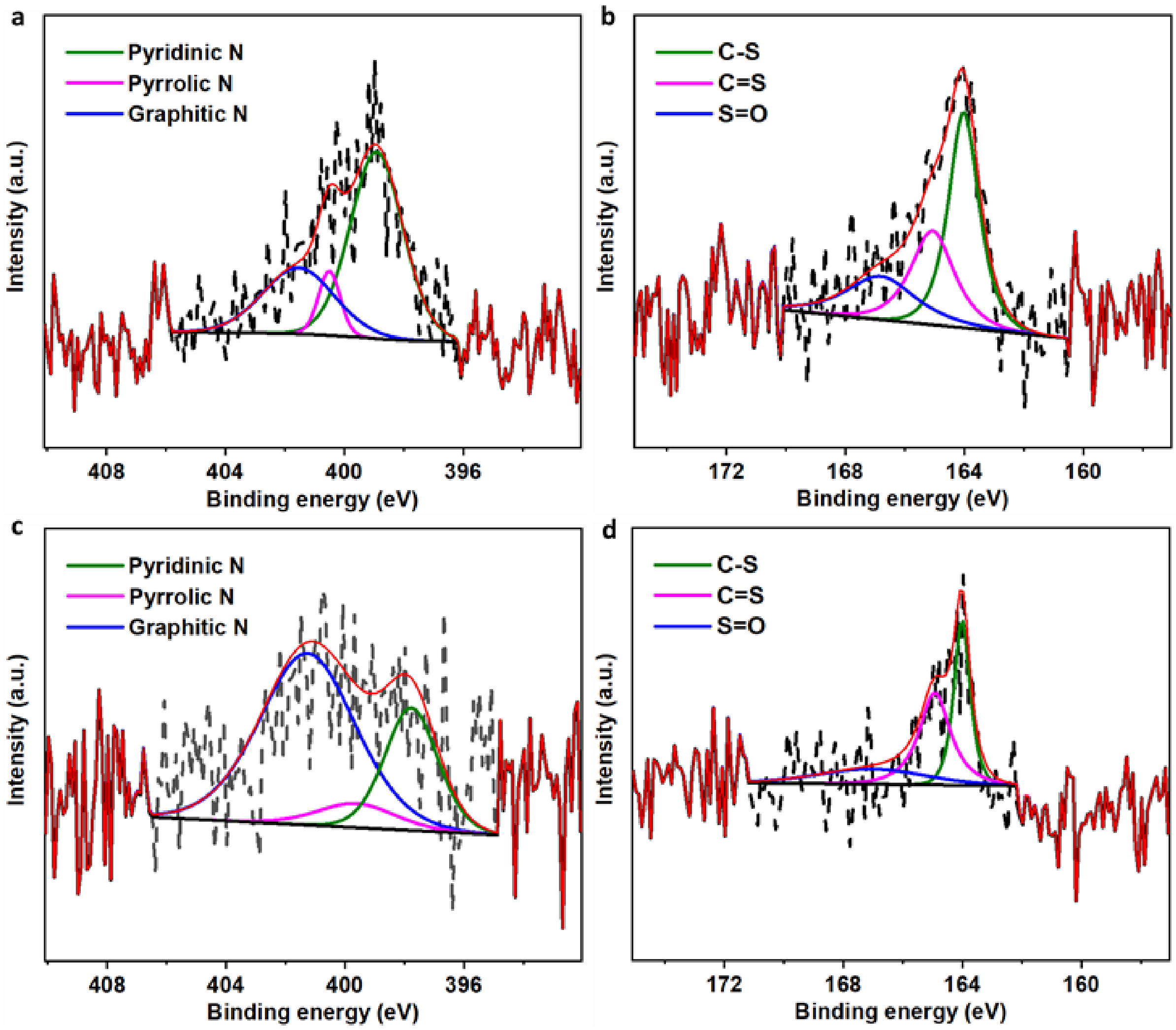

Figure S18. High resolution XPS spectra of NS-CD@gf_800 (a-b); (a) N 1s, and (b) S 2p. Elemental XPS spectra of NS-CD@gf_a1000 (c-d); (c) N 1s, and (d) S 2p.

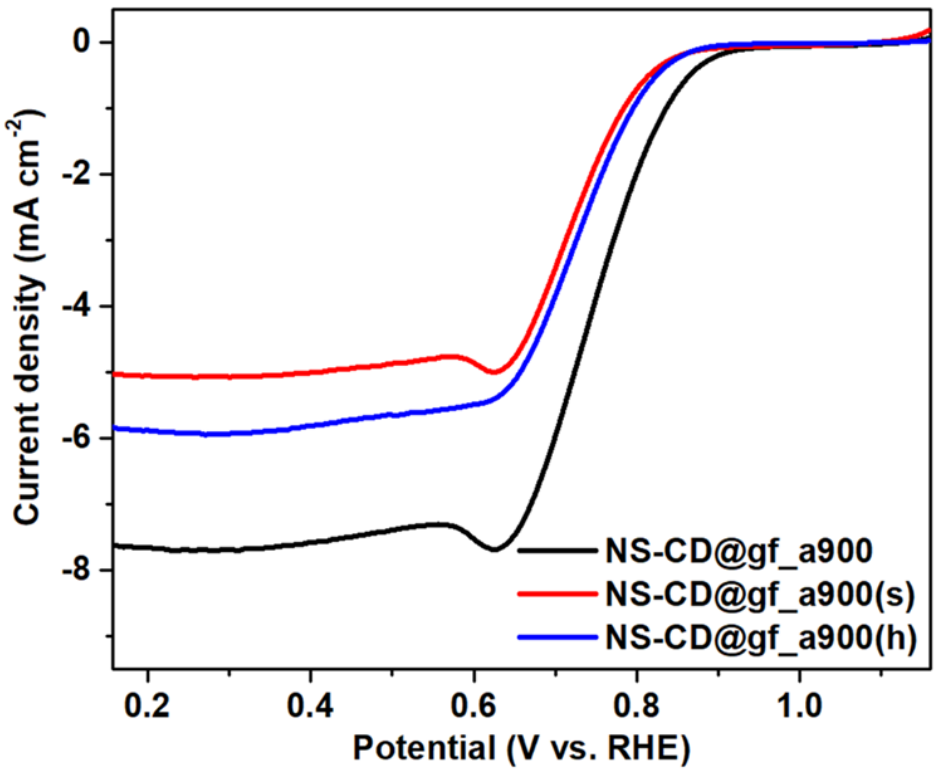

Figure S19. ORR LSV curves of NS-CD@gf_a900, NS-CD@gf_a900(s) with halved CD amount, and NS-CD@gf_a900(h) with doubled CD amount in 0.1 M KOH with rotation of 1600 rpm.

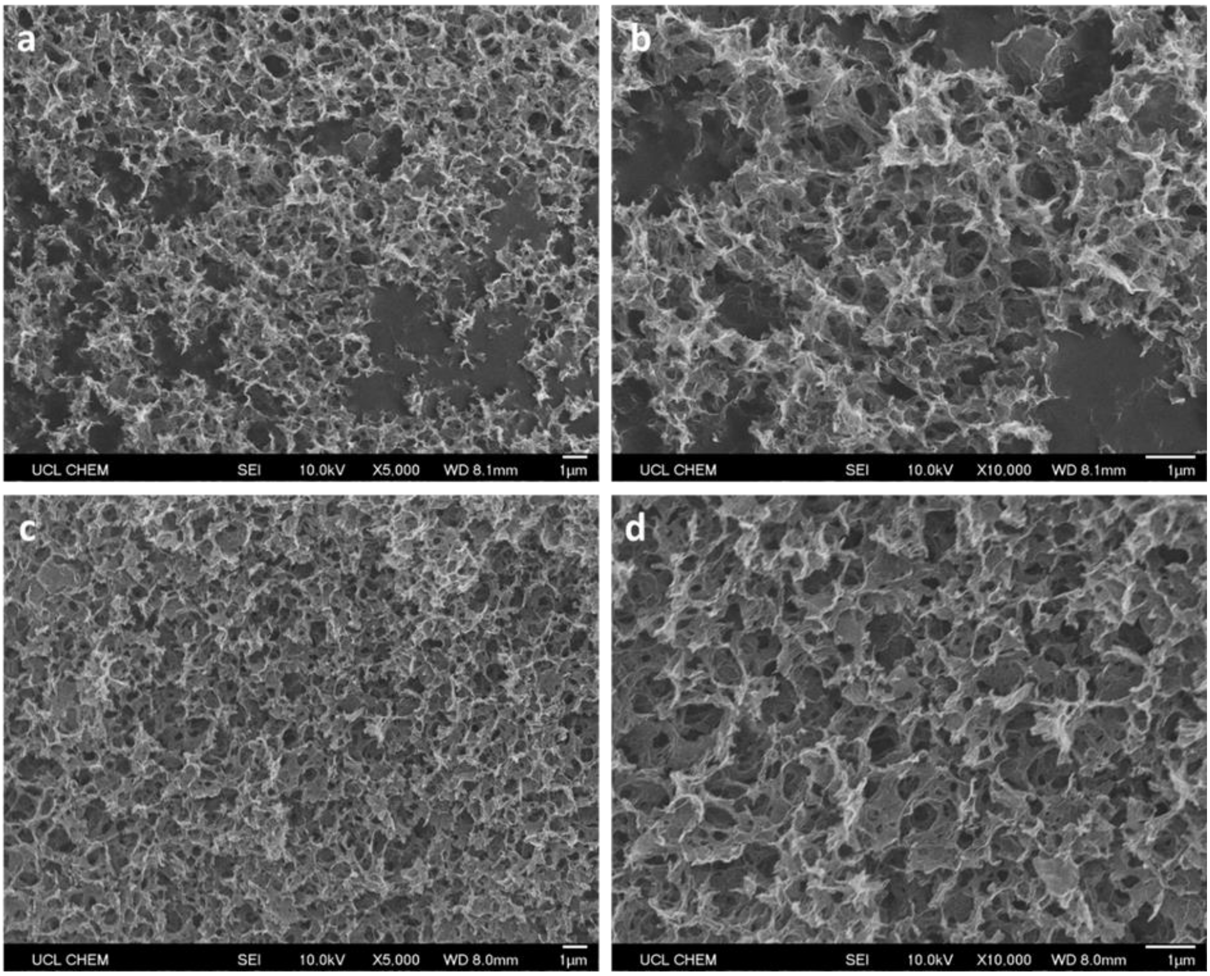

Figure S20. SEM images of NS-CD@gf_a900(s) in (a) low, (b) high, and NS-CD@gf_a900(h) in (c) low, and (d) high magnification.

Table S5. Total BET surface area and pore volume for CD-amout controlled samples.

Sample	**BET surface area (m^2 g^{-1})**	**Total pore volume (cm^3 g^{-1})**
NS-CD@gf_a900(s)	545.12	3.07
NS-CD@gf_a900(h)	428.34	2.15

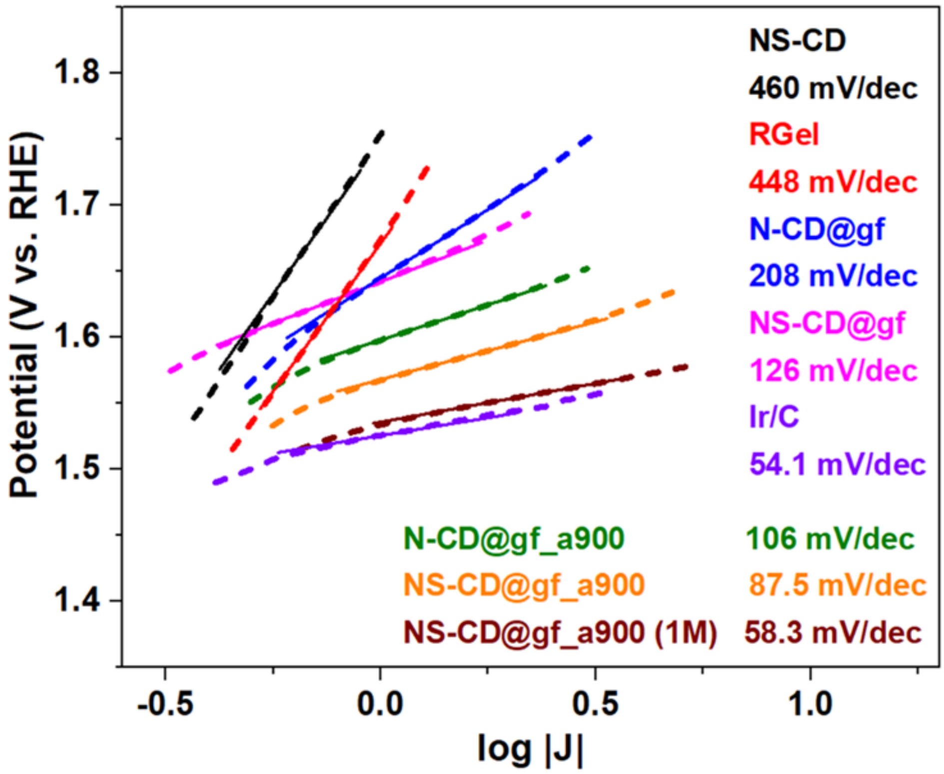

Figure S21. OER Tafel plots of all samples in 0.1 M KOH solution.

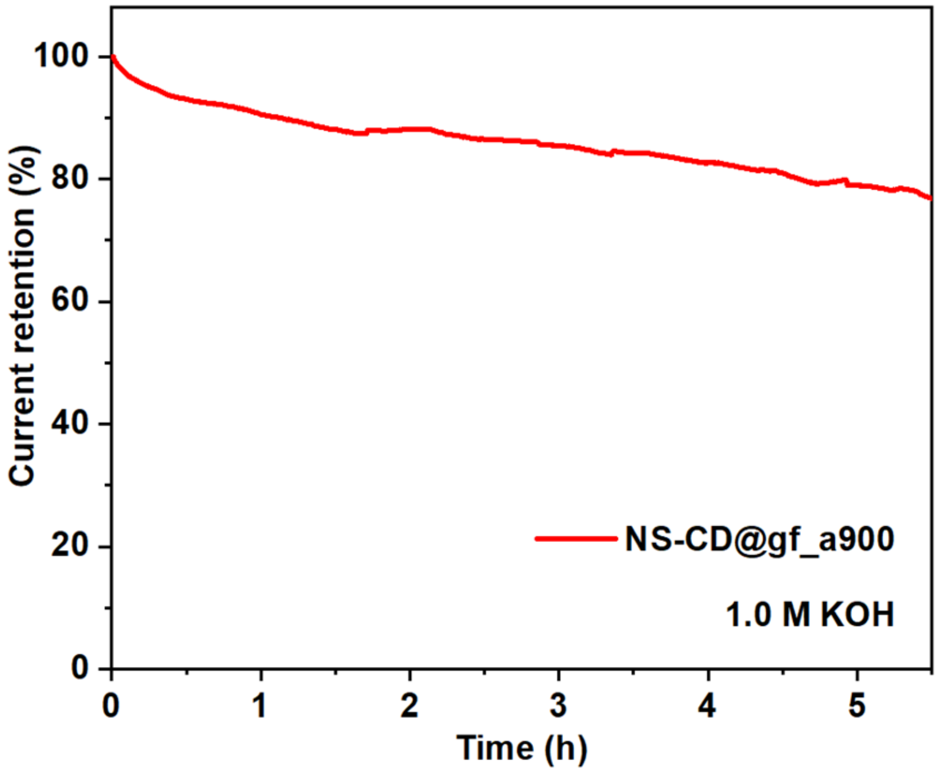

Figure S22. Chronoamperometric stability plot (*i* vs. time) of NS-CD@gf_a900 in 1.0 M KOH solution in the OER region with fixed rotation at 1600 rpm.

Table S6. Comparison of ORR/OER activity of oxygen electrocatalysts in 0.1 M KOH

Catalyst material	Mass loading (mg cm^{-2})	ORR (V vs.RHE)		OER (V vs. RHE)		ORR Limiting current density at 1600 rpm (mA cm^{-2})	Bifunctionality $\Delta E = E_{j10}$-E_{j3} (V vs. RHE)	Ref.
		E_{onset}	$E_{1/2}$ (E_3)	E_{onset}	E_{j10}			
Co embedded N-doped Carbon	0.25	0.83	0.74	~1.51	1.60	5.26	0.86	[1]
N-doped Co_9S_8 on graphene	0.2	0.94	0.76	1.51	1.64	~6.0	0.88	[2]
Co-N-C@ N-doped carbon	0.4	0.92	0.82	~1.52	1.64	~5.3	0.82	[3]
Fe-N on porous N-doped carbon	0.14	0.99	0.86	—	1.63	5.95	0.77	[4]
CoP nanoparticle defective carbon	0.36	~0.90	0.81	~1.51	1.55	~5.5	0.76	[5]
Ni-MnO on rGO aerogel	0.13	0.94	0.78	~1.49	1.60	~6.0	0.82	[6]
Co encapsulated N-doped carbon nanotube	0.2	0.97	0.9	~1.51	1.69	~5.8	0.79	[7]
Co confined in N-doped carbon foam	0.2	0.92	0.82	1.63	1.66	~5.5	0.84	[8]
S, S-bidoped CNT	0.23	0.87	0.79	~1.45	1.58	~3.5	0.79	[9]
Defective graphene	0.28	0.91	0.76	—	1.60	~4.6	0.84	[10]
N-doped graphene mesh	0.25	0.89	0.77	—	1.67	7.5	0.90	[11]
N-doped graphene @SWCNT	0.25	0.88	0.63	1.50	1.63	~4.9	1.00	[12]
N, S-doped porous carbon	0.42	0.99	0.88	1.30	1.69	5.8	0.81	[13]
CNT/Boron nitride nanocomposite	0.08	0.86	0.72	1.61	1.81	5.78	1.09	[14]
N, P-codoped CNT on graphene	0.3	0.91	0.79	~1.56	1.69	~5.2	0.90	[15]
N-doped porous carbon nanofiber films	0.1	0.97	0.82	1.43	1.84	4.7	1.02	[16]
N-doped graphene nanoribbons	0.6	0.92	0.84	1.53	1.66	~3.5	0.82	[17]
L-CVD assisted N-doped CNT	—	0.93	0.74	—	1.68	~4.2	0.94	[18]
N-CD@gf_a900	0.28	0.91	0.74 (0.75)	1.55	1.74	6.44	1.00 (0.99)	this work
NS-CD@gf_a900 NS-CD@gf_a900(1M)	0.28	0.93	0.75 (0.77)	1.52 (1.49)	1.68 (1.59)	7.71	0.93 (0.91) (0.82)	this work

*Unless both $E_{1/2}$ and E_{j3} values are provided, either $E_{1/2}$ or E_{j3} used to obtain ΔE values for comparison.

Supplementary References

[1] Y. Su, Y. Zhu, H. Jiang, J. Shen, X. Yang, W. Zou, J. Chen, C. Li, Nanoscale 2014, 6, 15080.

[2] S. Dou, L. Tao, J. Huo, S. Wang, L. Dai, Energy & Environmental Science 2016, 9, 1320.

[3] S. Liu, Z. Wang, S. Zhou, F. Yu, M. Yu, C. Y. Chiang, W. Zhou, J. Zhao, J. Qiu, Adv Mater 2017, 29.

[4] L. Ma, S. Chen, Z. Pei, Y. Huang, G. Liang, F. Mo, Q. Yang, J. Su, Y. Gao, J. A. Zapien, C. Zhi, ACS Nano 2018, 12, 1949.

[5] Y. Lin, L. Yang, Y. Zhang, H. Jiang, Z. Xiao, C. Wu, G. Zhang, J. Jiang, L. Song, Advanced Energy Materials 2018.

[6] G. Fu, X. Yan, Y. Chen, L. Xu, D. Sun, J. M. Lee, Y. Tang, Adv Mater 2018, 30.

[7] T. Wang, Z. Kou, S. Mu, J. Liu, D. He, I. S. Amiinu, W. Meng, K. Zhou, Z. Luo, S. Chaemchuen, F. Verpoort, Advanced Functional Materials 2018, 28.

[8] H. Jiang, Y. Liu, W. Li, J. Li, Small 2018, 14, e1703739.

[9] A. M. El-Sawy, I. M. Mosa, D. Su, C. J. Guild, S. Khalid, R. Joesten, J. F. Rusling, S. L. Suib, Advanced Energy Materials 2016, 6.

[10] Y. Jia, L. Zhang, A. Du, G. Gao, J. Chen, X. Yan, C. L. Brown, X. Yao, Adv Mater 2016, 28, 9532.

[11] C. Tang, H. F. Wang, X. Chen, B. Q. Li, T. Z. Hou, B. Zhang, Q. Zhang, M. M. Titirici, F. Wei, Adv Mater 2016, 28, 6845.

[12] G. L. Tian, M. Q. Zhao, D. Yu, X. Y. Kong, J. Q. Huang, Q. Zhang, F. Wei, Small 2014, 10, 2251.

[13] Z. Pei, H. Li, Y. Huang, Q. Xue, Y. Huang, M. Zhu, Z. Wang, C. Zhi, Energy & Environmental Science 2017, 10, 742.

[14] I. M. Patil, M. Lokanathan, B. Ganesan, A. Swami, B. Kakade, Chemistry 2017, 23, 676.

[15] B. Fang, J. Yang, C. Chen, C. Zhang, D. Chang, H. Xu, C. Gao, ChemCatChem 2017, 9, 4520.

[16] Q. Liu, Y. Wang, L. Dai, J. Yao, Adv Mater 2016, 28, 3000.

[17] H. B. Yang, J. Miao, S. Hung, J. Chen, H. B. Tao, X. Wang, L. Zhang, R. Chen, J. Gao, H. M. Chen, L. Dai, B. Liu, Science Advances 2016, 2.

[18] R. M. Yadav, J. Wu, R. Kochandra, L. Ma, C. S. Tiwary, L. Ge, G. Ye, R. Vajtai, J. Lou, P. M. Ajayan, ACS Appl Mater Interfaces 2015, 7, 11991.

Click here to access/download
Production Data
F1.tif

Click here to access/download
Production Data
F2.tif

Click here to access/download
Production Data
F3.tif

Click here to access/download
Production Data
F4.tif

Click here to access/download
Production Data
FS1.tif

Click here to access/download
Production Data
FS10.tif

Click here to access/download
Production Data
FS11.tif

Click here to access/download
Production Data
FS12.tif

Click here to access/download
Production Data
FS13.tif

Click here to access/download
Production Data
FS14.tif

Click here to access/download
Production Data
FS15.tif

Click here to access/download
Production Data
FS16.tif

Click here to access/download
Production Data
FS17.tif

Click here to access/download
Production Data
FS18.tif

Click here to access/download
Production Data
FS19.tif

Click here to access/download
Production Data
FS2.tif

Click here to access/download
Production Data
FS20.tif

Click here to access/download
Production Data
FS21.tif

Click here to access/download
Production Data
FS22.tif

Click here to access/download
Production Data
FS3.tif

Click here to access/download
Production Data
FS4.tif

Click here to access/download
Production Data
FS5.tif

Click here to access/download
Production Data
FS6.tif

Click here to access/download
Production Data
FS7.tif

Click here to access/download
Production Data
FS8.tif

Click here to access/download
Production Data
FS9.tif

Click here to access/download
Production Data
TOC.tif